Revision 1

High spatial resolution analysis of the Iron oxidation state in silicate glasses using the electron probe

Ery C. Hughes[1,*], Ben Buse[1], Stuart L. Kearns[1], Jon D. Blundy[1], Geoff Kilgour[2], Heidy M. Mader[1], Richard A. Brooker[1], Robert Balzer[3], Roman E. Botcharnikov[3,4], Danilo Di Genova[1], Renat R. Almeev[3], and Jenny M. Riker[1]

1 School of Earth Sciences, University of Bristol, Wills Memorial Building, Queens Road, Bristol BS8 1RJ, United Kingdom

2 GNS Science, Wairakei Research Centre, 114 Karetoto Road, RD4, Taupo 3384, New Zealand

3 Leibniz Universität Hannover, Institut für Mineralogie, Callinstrasse 3, D-30167, Hannover, Germany

4 Institute für Geowissenschaften, Johannes Gutenberg Universität Mainz, J.-J.-Becher-Weg 21, 55128 Mainz, Germany

* Corresponding author. Email: ery.hughes@bristol.ac.uk

Abstract

The iron oxidation state in silicate melts is important for understanding their physical properties, although it is most often used to estimate the oxygen fugacity of magmatic systems. Often high spatial resolution analyses are required, yet the available techniques, such as μXANES and μMössbauer, require synchrotron access. The Flank Method is an electron probe technique with the potential to measure Fe oxidation state at high spatial resolution, but requires careful method development to reduce errors related to sample damage, especially for hydrous glasses. The intensity ratios derived from measurements on the flanks of Fe Lα and Lβ X-rays (Fe $L\beta_f/L\alpha_f$) over a time interval (Time-Dependent Ratio

Flank Method) can be extrapolated to their initial values at the onset of analysis. We have developed and calibrated this new method using silicate glasses with a wide range of compositions (43 – 78 wt% SiO_2, 0 – 12 wt% H_2O, and 2 – 17 wt% FeO_T, which is all Fe reported as FeO), including 68 glasses with known Fe oxidation state. The Fe oxidation state (Fe^{2+}/Fe_T) of hydrous (0 – 4 wt% H_2O) basaltic (43 – 56 wt% SiO_2) and peralkaline (70 – 76 wt% SiO_2) glasses with FeO_T > 5 wt% can be quantified with a precision of ±0.03 (10 wt% FeO_T and 0.5 Fe^{2+}/Fe_T) and accuracy of ±0.1. We find basaltic and peralkaline glasses each require a different calibration curve, and analysis at different spatial resolutions (~20 and ~60 μm diameter regions respectively). A further 49 synthetic glasses were used to investigate the compositional controls on redox changes during electron beam irradiation, where we found that the direction of redox change is sensitive to glass composition. Anhydrous alkali-poor glasses become reduced during analysis, whilst hydrous and/or alkali-rich glasses become oxidised by the formation of magnetite nanolites identified using Raman Spectroscopy. The rate of reduction is controlled by the initial oxidation state, whereas the rate of oxidation is controlled by SiO_2, Fe, and H_2O content.

Key words: electron probe micro-analysis (EPMA), iron (Fe) oxidation state, Flank Method, electron beam damage, silicate glasses, oxidation, reduction, Raman spectroscopy.

Introduction

Oxygen fugacity is an important control on the chemical and physical properties of silicate melts, the stability of magmatic phases and the multiphase rheology of magmas (e.g., Hamilton et al., 1964; Dingwell and Virgo, 1987; Kress and Carmichael, 1991; Vicenzi et al., 1994; Bouhifd et al., 2004; Wilke, 2005). It also determines the valence state of multivalent

elements, such as Fe, Mn, Cr, V, Ce, Eu, and S, hence the ratio of oxidised to reduced species in the glasses quenched from melts provides a proxy for oxygen fugacity during natural processes and laboratory experiments (e.g., Carmichael, 1991; Kress and Carmichael, 1991; Herd, 2008). Many petrological and volcanological applications, such as analysis of glassy melt inclusions in minerals from volcanic rocks or interstitial glass in natural and experimental vesiculated and/or partially crystalline samples, require measurements at high spatial resolutions.

There are various techniques for quantifying the Fe oxidation state of silicate glasses, with trade-offs between resolution, error, sample preparation requirements, necessity for standards, and instrument accessibility (see McCammon, 1999). Wet chemistry is a destructive bulk technique, requiring a minimum of 5 mg of material (e.g., Schuessler et al., 2008), which does not require standards but some expertise. Synchrotron-based absorption techniques, such as μXANES (> 2 × 2 μm, e.g., Cottrell et al., 2018) and μMössbauer (> 10 × 5 μm, e.g., Potapkin et al., 2012) allow high spatial resolution analysis, but the need for access to synchrotron facilities limits their utility. Also, μXANES can oxidise Fe in hydrous glasses during analysis, producing erroneous Fe oxidation state values (Cottrell et al., 2018). Raman spectroscopy also has high spatial resolution (1 μm diameter), but has lower sensitivity for basaltic compositions and problems related to background fluorescence (e.g., Di Muro et al., 2009; Di Genova et al., 2016). Electron energy loss spectroscopy (EELS) would offer superior spatial resolution (nm) but standards are inhomogeneous at this scale and beam damage is significant (Burgess et al., 2016).

Conversely, the electron probe is widely available and has the potential for routine analysis of Fe oxidation state in geological materials (mainly garnet and amphibole) at high spatial resolution (Hofer et al., 1994; Enders et al., 2000; Hofer and Brey, 2007; Creighton et al., 2009, 2010; Malaspina et al., 2010; Lamb et al., 2012; Matjuschkin et al., 2014) but also

glasses (Fialin et al., 2001, 2004, 2011). Typically, the electron probe uses the intensity of emitted characteristic X-rays to quantify chemical composition, such as Fe Kα to quantify Fe concentration (Figure 1a), however a variety of other factors can affect the intensity of characteristic X-rays. The Fe Lα and Lβ lines are sensitive to the Fe oxidation state as their X-ray generation involves outer shell electrons (3d) affected by chemical bonding (Figure 1a) (Gopon et al., 2013). The energy of X-ray emission and absorption associated with the Fe L lines are very similar, which leads to self-absorption. The Fe Lα and Lβ peaks coincide with the L_3 and L_2 absorption edges respectively, and hence are distorted by them, resulting in asymmetric peak shapes and peak shifts due to the differing amounts of absorption on each side of the absorption edges (Smith and O'Nions, 1971). The wavelength of the energy of the absorption edges shift due to changes in the coordination and oxidation state of Fe (de Groot, 2001; Hofer and Brey, 2007). The L_3 absorption edge shifts more than the L_2 absorption edge, resulting in greater changes to the Fe Lα peak than the Fe Lβ (Hofer and Brey, 2007). Thus, for a given chemical system (e.g., garnet, olivine, silicate glass), the Fe Lα and Lβ peak positions and intensities vary depending on Fe concentration, oxidation state, and coordination (Figure 1b; Hofer and Brey, 2007).

There are two EPMA methods that exploit variations in Fe Lα and Lβ to quantify Fe oxidation state (Figure 1b). The Peak Shift Method uses the linear relationship between the wavelength of the Fe Lα peak with Fe oxidation state at a given FeO_T (Hofer et al., 1994; Fialin et al., 2004) (Figure 1b). To measure the Fe Lα peak position, wavescans across the Fe Lα peak are collected and a peak-fitting algorithm is applied to locate its wavelength. This method has been applied to silicate glasses with a statistical error on Fe^{2+}/Fe_T of ±0.05, although the error on individual analyses was greater (Fialin et al., 2004). Alternatively, the Flank Method uses changes in the wavelength and intensity of both the Fe Lα and Lβ peaks by measuring the intensity ratio of positions on the low wavelength flank of Fe Lα (Fe $L\alpha_f$)

and high wavelength flank of Fe Lβ (Fe $L\beta_f$), termed Fe $L\beta_f/L\alpha_f$ (Hofer et al., 1994; Hofer, 2002; Hofer and Brey, 2007) (Figure 1b). These flank positions coincide with the L_2 and L_3 absorption edges and, as the Fe^{2+} content changes, the L_3 absorption edge shifts. The sensitivity of the Flank Method results from the opposite sense of intensity change at each of the flank positions, as Fe $L\alpha_f$ is on the high absorption side of the L_3 absorption edge, whereas Fe $L\beta_f$ is on the low absorption side of the L_2 absorption edge, which utilises changes in both peak position and intensities (Hofer et al., 1994). Optimum flank positions can be found by collecting absorption spectra or using the maximum and minimum in the difference spectrum between samples with different Fe concentration and oxidation states (Figure 1b, Hofer and Brey, 2007). The Fe $L\beta_f/L\alpha_f$ intensity ratio is dependent primarily on total ferrous iron (Fe^{2+}), with a secondary dependence on total Fe (Fe_T), hence $Fe^{2+} = A + B\cdot(\text{Fe } L\beta_f/L\alpha_f) + C\cdot Fe_T + D\cdot Fe_T\cdot(\text{Fe } L\beta_f/L\alpha_f)$, where A, B, C and D are fitting coefficients (Hofer and Brey, 2007). The Flank Method has greater sensitivity than the Peak Shift Method and does not require wavescans as measurements are made at two specific, pre-defined wavelengths (Hofer et al., 1994; Zhang et al., in press). This method has been applied to some mineral groups (e.g., garnet, spinel) with an error on Fe^{2+}/Fe_T of ±0.02 (Hofer and Brey, 2007) and silicate glasses to within ±0.1 (Zhang et al., in press).

The Fe L lines have low intensity and therefore high beam currents and/or long count times are required to record them. Silicate glasses are typically unstable under these conditions, leading to changes in Fe oxidation state during analysis (Fialin et al., 2004, 2011; Fialin and Wagner, 2012; Zhang et al., in press). Similar problems have also been observed for Fe in amphiboles (Wagner et al., 2008; Lamb et al., 2012) and S in silicate glasses and anhydrite (Wallace and Carmichael, 1994; Rowe et al., 2007; Klimm et al., 2012). Fialin and Wagner (2012) observed two competing mechanisms of redox change during electron beam irradiation of alkali-bearing silicate glasses leading to either oxidation or reduction. As

glasses are insulators, electrons are trapped within the subsurface during electron beam irradiation, causing a region of negative charge to build-up at depth in the sample, even with a conductive coat (e.g., Cazaux, 1996). Alkali ions (predominantly Na^+, but also K^+) migrate towards the region of negative charge (e.g., Humphreys et al., 2006) leaving behind interstitial O^{2-} that migrates and either outgasses or combines with two FeO precipitating Fe_2O_3, thus causing oxidation (e.g., Lineweaver, 1963). This is different to oxidation processes driven by changes in oxygen fugacity. For basaltic glasses, Fe^{3+} is stabilised by the migration of Na^+ and K^+ towards them preventing Fe_2O_3 precipitation (Cooper et al., 1996). Concurrently, during electron beam irradiation electrons move away from the negatively charged region from O to Fe^{3+} sites resulting in net reduction (Nishida, 1995).

To minimise beam damage and prevent redox changes a sample can be moved during analysis, which reduces the electron dose per unit area (Metrich and Clocchiatti, 1996; Rowe et al., 2007; Fialin et al., 2011; Zhang et al., in press). Unfortunately, this requires large regions of glass for analysis making it unfeasible for analysing small areas, such as melt inclusions and interstitial glasses. Therefore, we adapt the Flank Method for high spatial resolution analysis of silicate glasses due to its greater sensitivity and the ability to measure at single spectrometer positions (Hofer et al., 1994). This is important because it is easier to measure time-dependent changes at specific wavelengths rather than using wavescans, as required for the Peak Shift Method. We measured Fe $L\beta_f/L\alpha_f$ over time, based on the Time-Dependent Intensity (TDI) technique first developed for alkali migration during EPMA of glasses by Nielsen and Sigurdsson (1981). Fe $L\beta_f/L\alpha_f$ is extrapolated to time zero to correct for changes over time, which we refer to as the Time-Dependent Ratio (TDR) correction, comparable to TDI corrections for alkalis. Due to the small sample size of silicate glasses analysed by Fialin and Wagner (2012) and Zhang et al. (in press), the controls on Fe redox processes during electron beam irradiation have not been explored and, crucially, few

hydrous glasses have been analysed. Therefore, we also investigate the compositional and analytical controls on Fe redox changes.

Samples

Silicate glasses of known (68 samples) and unknown (47 samples) Fe oxidation state from a variety of studies were mounted in epoxy and carbon coated (~15 nm thickness). The sample set covers a wide compositional range (anhydrous normalised SiO_2 43 – 78 wt%, Total Alkalis ($Na_2O + K_2O$) 1 – 12 wt%, and H_2O 0 – 12 wt%; Figure 2a and Table 1), which are used to investigate the effect of composition on Fe oxidation state changes during analysis. Silicate glasses of known Fe oxidation state (independently measured using wet chemistry, Mössbauer or μXANES), spanning 0.1 - 1.0 Fe^{2+}/Fe_T and 2 – 18 wt% FeO_T (Figure 2b), are used to calibrate the technique.

There are 16 suites of experimental silicate glasses that have different average glass compositions with variable Fe oxidation state and/or H_2O. The normalised (volatile-free) average glass compositions, which are either taken from the literature or measured using EPMA (see Supplementary Material for details and individual sample compositions) are given in Table 1. AR samples are anhydrous, low-silica glasses with a range of glass compositions: KLA-1-6-22 (Fuchs et al., 2014), SC1 (Botcharnikov et al., 2008), 140ox (Almeev et al., 2007), LS (previously unpublished studies conducted at the Institut für Mineralogie, Leibniz Universität Hannover, Germany), PF22 (Wengorsch et al., 2012), and BezBA (Almeev et al., 2013). These glass compositions were re-synthesised at various oxygen fugacities and analysed using wet chemistry by Zhang et al., (in press), where they have been analysed by the Flank Method using a moving stage approach. Hydrous, low-silica glasses are GRN (Stamper et al., 2014), ETNA (this study), MAS.1.A, MAS.1.B and St8.1.B

(Lesne et al., 2011), and AMS (Di Genova et al., 2014). GRN samples may have suffered oxidation during μXANES (Cottrell et al., 2018), therefore their reported Fe oxidation state values are not considered further and the samples are only used to explore the effects of composition on redox changes during EPMA. The high-silica glasses range from peralkaline (FSP; Di Genova et al., 2016, and PSG; Di Genova et al., 2013) to calcalkaline (Y; Di Genova et al., 2017a, and PSB; Riker et al., 2015), with both anhydrous (FSP and Y) and hydrous (PSG and PSB) glasses.

Additional anhydrous, low-silica glasses analysed are AII and LW (Cottrell et al., 2009), Smithsonian microbeam natural basaltic glass standards VG2 and VGA99 (Jarosewich et al., 1980) and PU (Ulmer, 1989; Blundy et al., 2018). Compositions are given in the Supplementary Material.

Methods

Fe L wavescans

Wavescans of the Fe L peaks on glasses with varying FeO_T and Fe oxidation state (Table 2) were analysed to examine the controls on peak position and intensity. Data were collected on the JEOL JXA 8530F Hyperprobe at the School of Earth Sciences, University of Bristol, UK, using a 50 nA beam current, 10 μm beam diameter, and 15 or 30 kV accelerating voltage. Three spectrometers, with two TAP and one TAPH crystals, were moved 0.071 mm per step for 100 steps with 0.5 s dwell time over the Fe L peaks whilst the stage moved at 1 $\mu m \cdot s^{-1}$ to minimise beam damage. To improve signal to noise ratio, multiple wavescans (40 – 80, depending on the accelerating voltage and glass FeO_T) were collected, and the spectra from the three spectrometers were combined to produce a single wavescan per sample.

Time-Dependent Ratio Fe $L\beta_f/L\alpha_f$ measurements

Selecting flank positions. To identify the optimum flank positions for Fe $L\beta_f/L\alpha_f$, the method of Hofer and Brey (2007) (described in the Introduction, Figure 1b) was used. Two spectra, representing the range of FeO_T and Fe oxidation state (AR14 and AR19, Figure 3a), were normalised to the maximum intensity of their Fe Lα peak from which the difference spectrum was calculated (AR14 – AR19, Figure 3c). Optimum flank positions correspond to the maximum (low wavelength flank of Fe Lα, Fe $L\alpha_f$) and minimum (high wavelength flank of Fe Lβ, Fe $L\beta_f$) of the difference spectrum. To avoid collecting wavescans on these glasses every session, the flank positions were measured relative to the F Kα peak measured on MgF_2 for each TAP/TAPH crystal. This reduced the time required to find the flank positions during future analytical sessions and minimised the area damaged by electron beam irradiation.

Electron probe set-up. Each spectrometer measured a single wavelength and the spectrometer set-up (referred to by crystal) was two TAP crystals to measure Fe $L\alpha_f$, TAPH for Fe $L\beta_f$, LLIF for Fe Kα, and PETH for K Kα. At the wavelengths of interest, the TAPH crystal offers twice the peak intensity of the TAP crystals, and the Fe Lβ has roughly half the intensity of the Fe Lα peak, therefore we chose the above combination of spectrometers to maximise count rates. The full-width half-maximum wavelength resolution for F Kα in MgF_2 here is 0.0813, 0.0835, and 0.1034 Å (0.8792, 1.1235, and 0.9079 mm spectrometer units) for the two TAP and TAPH crystals respectively (Buse and Kearns, 2018). Differential Pulse Height Analysis (PHA) mode was used to remove interferences such as the 9^{th} order Fe Kα, and PHA scans were collected every session on each spectrometer on F Kα in MgF_2. Na is typically the most mobile element measured during electron beam irradiation and therefore commonly used to monitor beam damage. However, in the absence of an additional TAP crystal, we measured K (also highly mobile) instead on a PETH crystal. For each analytical session, Fe Kα was peaked-up on BCR-2 (USGS basaltic glass standard), K Kα on sanidine, and the peak position of F Kα was measured on MgF_2 to calculate the wavelengths of the

225 flank positions on each TAP/TAPH crystal. Spectrometers were static during analysis as
226 backgrounds are not required for flank analyses (Hofer et al., 1994). As no other elements (or
227 backgrounds) were measured, no matrix correction could be performed to quantify Fe or K,
228 thus only their relative intensity over time is used. Analytical conditions were a 15 kV
229 accelerating voltage, 50 nA beam current, and 4 – 15 μm beam diameter, which allows the
230 analysis of small volumes of glass. Intensity measurements were collected over 5 s for a total
231 duration of ~ 150 s on the same spot of glass. Ten repeat analyses on fresh glass per sample
232 were collected, resulting in a total analysis area of ~20 – 60 μm diameter. Data were collected
233 over five sessions. A summary of the analytical protocol is provided in the Appendix.

234 **Redox stability.** To investigate the effect of analytical conditions on redox changes,
235 additional measurements were made at different analytical conditions (Table 3) on four
236 glasses chosen to represent the range of glass compositions studied (Table 4). AR10 and
237 AR16 are anhydrous low-silica glasses, that are oxidised and reduced respectively.
238 MAS.1.B4 and PSB63 are hydrous glasses that are low- and high-silica respectively.

239 **Data processing.** To check for sample homogeneity, Fe Kα was compared between repeat
240 analyses. If the Fe Kα intensity was significantly outside the counting error for other repeats,
241 the erroneous repeat analysis was removed from further processing and, if the sample was too
242 inhomogeneous, the sample was not processed further. The analyses were then averaged at
243 each time interval for Fe $L\alpha_f$ (separately for each spectrometer), Fe $L\beta_f$, Fe Kα and K Kα.
244 Using these averages at each time interval, Fe $L\beta_f$ was divided by the sum of Fe $L\alpha_f$ from the
245 two spectrometers to calculate Fe $L\beta_f/L\alpha_f$. Errors on Fe Kα, K Kα, Fe $L\beta_f/L\alpha_f$ and time are
246 the standard deviation of the repeat measurements. An exponential equation of the following
247 form was fitted to each sample:

248 $$I = (I_0 - I_\infty) exp\left(\frac{I_0' t}{I_0 - I_\infty}\right) + I_\infty \quad (1)$$

Where I is the Fe $L\beta_f/L\alpha_f$ intensity ratio and t is time, subscripts refer to the values at time = 0 and ∞, and I_0' is the rate of change of I with time at time = 0. When the minimisation failed to converge, I_∞ was fixed to the last measured value for the sample. The error in both these cases is the standard error on the fit coefficients. In those cases where Fe $L\beta_f/L\alpha_f$ was constant with time, convergence is not possible, therefore the average of Fe $L\beta_f/L\alpha_f$ with time was used, where the error was the standard deviation of these data. Analyses with large errors ($> \pm 0.1$ for I_0 and $> \pm 0.01$ for I_0'), likely due to inhomogeneity, extremely rapid redox changes or analytical problems, are discarded. An R code for data processing is included in the Supplementary Material.

Raman Spectroscopy

Raman spectroscopy was used to detect the presence of nanolites before and after electron beam irradiation as nanolites alter the Raman spectra of silicate glasses. Magnetite nanolites produce a peak due at ~670 cm^{-1}, which also decreases the intensity of the surrounding silicate peaks (Di Genova et al., 2017a,b). Carbon coats were removed prior to analysis. Raman spectra were collected using the Thermo Scientific DXRxi Raman Imaging Microscope at the School of Earth Sciences, University of Bristol, UK, with a green (520 nm) laser, 50× (long distance) or 100× objective, and 3 – 5 mW power to avoid sample oxidation. An extended grating was used to also collect data on H_2O content. All samples, except AMS, FSP, PSG, and Y which have been previously analysed by Di Genova et al. (2017a,b), were analysed on non-irradiated areas of glass. Selected glasses that cover a range of compositions (ETNA08, MAS.1.A5, FSP1, FSP9, PSG6, and PSB63) were additionally analysed following electron beam irradiation.

Results

Electron Probe Micro-Analysis

Wavelength and intensity changes of Fe L lines in silicate glasses. For the same Fe oxidation state, peak intensity increases and peak positions shift to higher wavelengths with increasing FeO_T (Figure 3a). For the same FeO_T oxidised samples have greater peak intensities and lower wavelength peak positions than reduced samples (Figure 3a). At higher accelerating voltages (30 vs. 15 kV) the intensity of Fe Lα and Fe Lβ decrease, but there is no appreciable shift in peak positions (Figure 3b). Therefore, there is no appreciable change in optimum flank positions, although the difference between the flank intensities decreases (Figure 3c).

Time-dependent intensity changes during electron beam irradiation. During electron beam irradiation, the intensity of K Kα remains stable (anhydrous glasses) or decreases (hydrous glasses) over time (Figure 4), whereas for Fe Kα the intensity remains stable (anhydrous glasses) or increases (hydrous glasses) (Figure 5). The ratio of Fe $L\beta_f/L\alpha_f$ increases (anhydrous low-silica), remains stable (anhydrous low-silica and hydrous high-silica) or decreases (hydrous low-silica) over time (Figure 6). In those cases where intensity changes are observed, the rate typically increases with decreasing beam diameter and accelerating voltage, and increasing beam current. Data were collected during different sessions, therefore differences in the absolute intensity at different conditions are not meaningful.

Raman spectroscopy

Before electron beam irradiation. The majority of glasses analysed are nanolite-free prior to electron beam irradiation (Figure 7a and b). Exceptions are AR37 (composition LS) and ETNA(2) (samples ETNA 3, 6, 7, 8, 14, 16 and 30), with a peak at ~670 cm^{-1} indicating

296 magnetite nanolites. Magnetite nanolites were detected in AMS4 and Y-L using Raman
297 spectroscopy by Di Genova et al. (2017a,b).

298 **After electron beam irradiation.** Most glasses analysed following electron beam irradiation
299 (MAS.1.A4, FSP1, FSP9 and PSG6) exhibit new magnetite nanolites (peak at ~670 cm^{-1}
300 wavenumbers) when irradiated using a 4 μm beam diameter implying oxidation (Figure 7c).
301 Additionally, ETNA08, MAS.1.A4, and PSG6 have a new peak at ~1350 cm^{-1}, which
302 corresponds to haematite (RUFF Raman spectra database, http://rruff.info/, Lafuente et al.,
303 2015), implying the formation of haematite nanolites following electron beam irradiation
304 (Figure 7c). PSB63 shows no evidence for the presence of Fe-bearing nanolites following
305 electron beam irradiation. The H_2O peak (~3600 cm^{-1}) shows a decrease in height after
306 electron beam irradiation for hydrous samples (ETNA08, MAS.1.A4, PSG6, and PSB63),
307 implying loss of water.

308

309 **Controls on Fe redox changes in silicate glasses during electron beam irradiation**

310 The ratio of Fe $L\beta_f/L\alpha_f$ over time increased, remained stable or decreased (Figure 6), which
311 could be due to a variety of causes as Fe $L\beta_f/L\alpha_f$ depends on Fe concentration, oxidation state
312 and coordination. Fe Kα increases over time (Figure 5), implying an increase in Fe_T. This is
313 due to the process of "grow-in" (Morgan and London, 2005), where the concentration of
314 immobile elements (e.g., Si, Al and Fe) increases due to the migration of alkalis (e.g., Na^+
315 and K^+, Figure 4) and H^+ (Figure 7c) towards the build-up of negative charge at depth (e.g.,
316 Humphreys et al., 2006) and possible density changes. The increase in Fe_T implied by the
317 increase in Fe Kα for hydrous silicate glasses (MAS.1.B4 and PSB63, Figure 5) is small
318 (~0.13 wt% FeO_T). This is calculated to cause a negligible change on Fe $L\beta_f/L\alpha_f$ (~0.004,

within measurement error), and therefore changes due to Fe concentration are not considered further.

Additional carbon contamination can be deposited on the sample during electron beam irradiation (Bastin and Heijligers, 1988). This can change X-ray intensities over time due to reduction of the electron landing energy caused by energy loss within and X-ray absorption by the contaminant (Reed, 1975). The former is negligible at the high voltages used here, whereas the latter should not affect Fe $L\beta_f/L\alpha_f$ as the mass absorption coefficients of Fe Lα and Fe Lβ by C are very similar (5762.34 and 5485.53 $cm^2 \cdot g^{-1}$ respectively from the FFAST database). To change Fe $L\beta_f/L\alpha_f$ by 1 % relative (within measurement error) would require > 100 nm of C contamination (calculated using CalcZAF) during the 150 s analysis. This is far more than has been measured in previous studies (e.g., 8 ± 2 nm over 180 s; Buse et al., 2016), therefore the effect of contamination can be considered negligible.

These considerations imply that any changes observed in Fe $L\beta_f/L\alpha_f$ are due primarily to changes in Fe oxidation state over time. Increasing Fe $L\beta_f/L\alpha_f$ is caused by increasing Fe^{2+}/Fe_T and hence Fe reduction ($Fe^{3+} \rightarrow Fe^{2+}$). Conversely, decreasing Fe $L\beta_f/L\alpha_f$ is caused by decreasing Fe^{2+}/Fe_T and hence Fe oxidation ($Fe^{2+} \rightarrow Fe^{3+}$). Finally, no change in Fe $L\beta_f/L\alpha_f$ with time implies stable Fe^{2+}/Fe_T during analysis. The presence of predominantly magnetite nanolites after electron beam irradiation implies that oxidation proceeds via precipitation of $FeO \cdot Fe_2O_3$, not just Fe_2O_3, as has been previously suggested (Fialin and Wagner, 2012).

Direction of redox change: Total Mobile Cations

To investigate the compositional controls on the rate and mechanism of redox changes during electron beam irradiation, we define the parameter Total Mobile Cations (TMC), which is the molar sum of (H_2O + Na_2O + K_2O) per gram of glass (units: $mol \cdot g^{-1}$). This provides a

maximum estimate of the moles of available oxygen if all the H^+, Na^+ and K^+ migrated due to the build-up of negative charge (Humphreys et al., 2006). TMC is typically dominated by H_2O due to the low atomic mass of H compared to Na and K. Figure 8 shows the rate of change of Fe $L\beta_f/L\alpha_f$ with time at time zero (I'_0) against TMC. Glasses with TMC < 0.1 $mol \cdot g^{-1}$ remain stable or reduce over time ($I'_0 \geq 0$ s^{-1}), corresponding to anhydrous (H_2O < 0.38 wt%), alkali-poor ($Na_2O + K_2O$ < 5.5 wt%) glasses. Conversely, glasses with TMC > 0.1 $mol \cdot g^{-1}$ remain stable or oxidise over time ($I'_0 \leq 0$ s^{-1}) corresponding to either hydrous (H_2O > 1.03 wt%) or alkali-rich (11.3 ± 0.2 wt% $N_2O + K_2O$) glasses. The mechanisms causing reduction are likely always to occur in the glass during electron beam irradiation, therefore it appears that at TMC ≥ 0.1 $mol \cdot g^{-1}$ the rate of oxidation is greater than the rate of reduction, hence oxidation prevails.

Rate of reduction: Initial Fe oxidation state

Figure 9 shows I'_0 against initial Fe^{2+}/Fe_T for anhydrous, low-silica (43 – 56 wt% SiO_2) glasses where, for a specific glass composition, Fe^{2+}/Fe_T correlates negatively with rate of reduction. Glasses that are mostly reduced (Fe^{2+}/Fe_T > 0.9) cannot reduce any further and remain stable, therefore reduction is confined to initially oxidised glasses. Between the suites of glass with different compositions, there is no obvious compositional control on I'_0.

Rate of oxidation

H_2O content. Figure 10 shows the rate of change of Fe $L\beta_f/L\alpha_f$ over time at time zero (I'_0) against TMC for suites of low-silica glasses (43 – 56 wt% SiO_2) that have variable H_2O concentrations, but constant glass composition. Broadly, I'_0 becomes more negative with increasing TMC. For a fixed glass composition the increase in TMC is due to increasing H_2O content, therefore the rate of oxidation increases with increasing H_2O. The diffusivity of H_2O in basaltic glasses is dependent on the total H_2O content (Okumura and Nakashima, 2006),

thus the rate of oxidation increases with increasing H_2O diffusivity. These results show that the migration of H^+, in addition to Na^+ and K^+ as previously suggested by Fialin and Wagner (2012), leads to oxidation of Fe during electron beam irradiation. In fact, when considering the mobile cation responsible for Fe oxidation, H^+ plays a more important role than might be expected from its oxide wt% concentrations alone due to the low atomic mass of H.

SiO_2 content. High-silica (61 – 78 wt% SiO_2) glasses remain broadly stable during electron beam irradiation (Figure 8), despite the Raman spectra of electron beam irradiated areas using a 4 μm beam diameter indicating the formation of magnetite nanolites (Figure 7c). This implies extremely rapid oxidation at 4 μm, which is consistent with the rate of alkali migration, and probably H, being faster during electron beam irradiation of high- compared to low-silica glasses (e.g., Figure 4; Hayward, 2011). This may be due to the more polymerised structure of high-silica glasses (Mysen et al., 1982).

Fe content. PSB glasses do not oxidise ($I'_0 \approx 0$ s^{-1}, Figure 8, and there are no Fe-bearing nanolites observable in the Raman spectra prior to or following electron beam irradiation, Figure 7c), despite TMC > 0.4 $mol \cdot g^{-1}$ due to their high alkali and water contents. These glasses contain little Fe ($FeO_T \leq 3.2$ wt%), which could hinder oxidation as FeO groups may need to lie close together in order to produce Fe_2O_3.

Presence of nanolites. Surprisingly, low-silica (47 – 58 wt% SiO_2) glasses with TMC > 0.35 $mol \cdot g^{-1}$, which corresponds to H_2O > 4 wt% (Figure 10), appear stable ($I'_0 \approx 0$ s^{-1}). It is possible that they oxidised very quickly and the change is not observable. Analyses using a 10 μm beam size are also stable (Figure 8a), but there is evidence for the formation of haematite nanolites during electron beam irradiation (Figure 7c). This either means the oxidation is extremely rapid, due to the very high H_2O contents, or not occurring due to the

presence of magnetite nanolites before irradiation where the Fe may be stable, but further study is required to understand this process fully.

Effect of analytical conditions

For all X-rays measured (K Kα, Fe Kα and Fe $L\beta_f/L\alpha_f$), the rate of change of intensity increases with decreasing beam diameter and accelerating voltage, and increasing beam current (Figure 4 – Figure 6, 8), as is commonly observed during electron beam irradiation (e.g., Morgan and London, 2005). The analytical conditions control the electron density implanted into the sample and therefore the magnitude of sub-surface charging. Increasing the beam current increases the electron dosage to the sample. The interaction volume is reduced by decreasing both the accelerating voltage and beam diameter, limiting the depth these electrons penetrate and the irradiated area respectively. Overall, the rate of intensity change increases with increasing implanted electron density (i.e., decreased interaction volume and/or increased electron dosage).

Quantifying Fe oxidation state: Time-Dependent Ratio Flank Method

Calibration and errors

Hofer and Brey (2007) found that the ratio of Fe $L\beta_f/L\alpha_f$ correlated linearly with Fe^{2+} for garnets, with a small secondary dependence on Fe_T. Consequently, their coefficients (*m* and *c*) of $Fe^{2+} = m\cdot(\text{Fe } L\beta_f/L\alpha_f) + c$ were dependent on Fe_T. Our data showed no improvement to the correlation between Fe $L\beta_f/L\alpha_f$ and Fe^{2+} by allowing the coefficients to depend on Fe_T, therefore *m* and *c* are fitted without Fe_T dependence using a weighted least squares regression (weighted using error on independently-constrained Fe^{2+}). The lack of dependence on Fe_T is likely because the composition of natural silicate glasses investigated here covers a much narrower range of Fe_T compared to garnets (< 18 vs. 64 wt% FeO_T respectively). The

414 calibration curve is not constant between sessions (Figure 11 and Table 5, and additional
415 sessions in the Supplementary Material), therefore a new calibration curve should be
416 produced for each session.

417 It appears that low-silica and peralkaline glasses require different calibration curves (Figure
418 11b), therefore these two sample groups were fitted separately. Using these different
419 calibration curves, Fe^{2+}/Fe_T is replicated well for both compositions (Figure 12a and b). Fe
420 coordination also effects the Fe L lines but the coordination of silicate glasses is very similar
421 (Cottrell et al., 2009). Instead, it may be that absorption within the glass of the Fe L lines is
422 different between these two broad compositional groups due to their different compositions,
423 although this was not observed for garnets (Hofer and Brey, 2007). Compositional
424 differences within the low-silica glasses may also explain the scatter observed in the
425 calibration curves, but it is not possible to explore this fully using the current dataset. It may
426 be that errors on Fe^{2+}/Fe_T can be reduced by using compositionally-matched glass standards.
427 In practice such standards are unlikely to be available, therefore we recommend using
428 standards with broadly similar compositions (i.e., low-silica or peralkaline) when using this
429 technique.

430 A calibration curve could not be created for high-silica glasses PSB and Y as they cover a
431 narrow range of Fe^{2+} (< 2 wt% Fe^{2+}). Their Fe^{2+}/Fe_T are poorly replicated by the low-silica
432 calibration curve (Figure 12c), to which they lie more closely than the peralkaline calibration
433 curve (Figure 11b). This is likely due to their low Fe content (FeO_T < 3.3 wt%, except Y-L
434 with 6.2 wt%), therefore this technique is unsuitable for low Fe glasses (i.e., FeO_T < 5 wt%).

435 The Fe^{2+}/Fe_T precision, using a residual standard error of 0.5 wt% on Fe^{2+} and 1 % relative
436 error on FeO_T, depends on the Fe concentration and oxidation state (Fe^{2+}/Fe_T error =
437 $(Fe^{2+}/Fe_T)_{EPMA} \cdot \sqrt{[(0.5/Fe^{2+})^2+(0.01)^2]}$), e.g., ±0.03 for 10 wt% FeO_T and 0.5 Fe^{2+}/Fe_T. The

438 average accuracy for low-silica (43 – 56 wt% SiO_2) and peralkaline (70 – 76 wt% SiO_2)
439 glasses with 5 – 18 wt% FeO_T, and 0 – 4 wt% H_2O, when the appropriate analytical
440 conditions and calibration curves are used, is ±0.1 (Figure 12a and b).

441 **Recommended analytical conditions**

442 Analytical conditions can be optimised according to the nature of any given sample as
443 different conditions (beam diameter and current, total count time of a single analysis, and
444 number of analyses averaged) can be used on the standards and unknowns, so long as the
445 accelerating voltage and flank positions remain the same. Hofer and Brey (2007) showed that
446 for garnets the optimum accelerating voltage is 15 kV; at lower and higher accelerating
447 voltages the sensitivity of the Flank Method is reduced. For glasses, the sensitivity of the
448 Flank Method also decreased at higher accelerating voltages (Figure 3b and c). An
449 accelerating voltage of 15 kV allows the composition of the sample to be analysed, via
450 conventional EPMA, without further calibration or beam focussing.

451 The error on the corrected Fe $L\beta_f/L\alpha_f$ is a function of counting statistics, the fit of an
452 exponential function to the change in Fe $L\beta_f/L\alpha_f$ with time, and the number of analyses
453 averaged. Counting statistics can be improved by using a higher beam current, but this can
454 cause the rate of change to occur too quickly to be observed. Decreasing the beam diameter
455 will also increase the rate of change, as seen here for high-silica glasses, but improves spatial
456 resolution. Therefore, it is important to know the approximate composition of the target glass
457 (e.g., by EDS analysis) to understand how quickly the change in Fe oxidation is likely to
458 occur. If redox changes occur too quickly, the time-corrected Fe $L\beta_f/L\alpha_f$ will be wrong
459 leading to erroneous Fe^{2+}/Fe_T values. Our data at a 15 kV accelerating voltage, 50 nA beam
460 current, 4 μm beam diameter, and averaging 10 analyses produced a relative error on the
461 corrected Fe $L\beta_f/L\alpha_f$ of ~3 %, and gave the flexibility to analyse a variety of glass

462 morphologies for hydrous low-silica glasses. A larger beam size (10 – 15 μm diameter) is
463 needed to analyse high-silica samples containing sufficient iron (i.e., peralkaline) due to the
464 rapid rate of oxidation, which unfortunately sacrifices spatial resolution. This technique may
465 not be appropriate if samples contain fine-scale heterogeneities (e.g., nanolites), as the Fe
466 coordination in these phases may differ to that in the glass.

467 **Further applications**

468 The TDR Flank Method presented here could be applied to other beam-sensitive samples.
469 Electron probe induced dehydrogenation has been observed for kaersutitic amphibole,
470 resulting in the underestimation of Fe^{2+}/Fe_T due to oxidation (Wagner et al., 2008). Wagner et
471 al. (2008) showed the severity of damage correlated with analytical conditions and H_2O
472 content of the amphibole, in much the same way as shown here for silicate glasses. Therefore,
473 applying the TDR Flank Method to amphiboles may provide robust Fe oxidation state
474 estimates without sacrificing spatial resolution.

475 Oxidation and reduction of S has been observed during analysis of silicate glasses and
476 anhydrite when using the S Kα peak shift to measure S oxidation state (Wallace and
477 Carmichael, 1994; Rowe et al., 2007; Wilke et al., 2011). Sulphur oxidation in silicate glasses
478 appeared to follow an exponential trend and, as observed here, the estimate of redox state at
479 time zero was found to agree with XANES measurements of the same sample (Wilke et al.,
480 2011). Sulphur redox changes are controlled by similar factors to Fe such as initial S
481 oxidation state (Rowe et al., 2007) and H_2O content (Wilke et al., 2008). If a Flank-type
482 method was developed for S (Wilke et al., 2011), time-dependent measurements could also
483 be applied, negating the need to move samples during analysis (Metrich and Clocchiatti,
484 1996; Rowe et al., 2007), thereby improving spatial resolution.

485

Implications

Measuring the Fe oxidation state of silicate melts allows estimation of oxygen fugacity prevailing during natural processes and in experiments. The Time-Dependent Ratio Flank Method presented here combines the ability to measure the Fe oxidation state at high resolution with the utility of the electron probe. This will allow routine measurement of Fe oxidation state of melt inclusions and interstitial glass, previously hampered by the need for synchrotron access. Melt inclusions provide a unique insight into the pre-eruptive magma but studies have shown that the Fe oxidation state can be altered by degassing (e.g., Moussallam et al., 2014) and cooling (e.g., Hartley et al., 2017) post-entrapment, complicating their use as a proxy for oxygen fugacity. Hence, larger datasets generated due to easier access, will allow the importance of these processes to be further investigated, although for some applications smaller errors will be required. Also, a better understanding of the analytical and compositional controls on redox changes during electron beam irradiation of silicate glasses (summarised in Figure 13) can aid our understanding of glass structure and improve analytical routines.

Acknowledgments

We thank Richard Hinton for his assistance at the NERC ion microprobe facility at the University of Edinburgh, UK (IMF560/0515). We thank Priscille Lesne, Charlotte Stamper, Peter Ulmer, and Liz Cottrell for providing samples. ECH is supported by a NERC GW4+ DTP studentship from the Natural Environment Research Council (NE/L002434/1) and is thankful for the support and additional funding from CASE partner GNS Science, New Zealand. GK acknowledges support from the New Zealand Strategic Science Investment Fund. HMM, RAB, and DDG were supported by the NSFGEO-NERC "Quantifying

disequilibrium processes in basaltic volcanism" (NE/N018567/1). RRA was supported by the German Science Foundation (DFG project AL 1189/6-1). We thank John Donovan and two anonymous reviewers for their helpful comments.

References

Almeev, R.R., Holtz, F., Ariskin, A.A., Kimura, J.-I., 2013. Storage conditions of Bezymianny Volcano parental magmas: results of phase equilibria experiments at 100 and 700 MPa. Contributions to Mineralogy Petrology, 166, 1389–1414.

Almeev, R.R., Holtz, F., Koepke, J., Parat, F., Botcharnikov, R.E., 2007. The effect of H_2O on olivine crystallization in MORB: Experimental calibration at 200 MPa. American Mineralogist, 92, 670–674.

Bastin, G.F., and Heijligers, H.J.M., 1988. Contamination phenomena in the electron probe microanalyzer. Microbeam Analysis: Proceedings of the Annual Conference of the Microbeam Analysis Soceity, 23, 325.

Berndt, J., Liebske, C., Holtz, F., Freise, M., Nowak, M., Zienbenbein, D., Hurkuck, W., and Koepke, J., 2002. A combined rapid-quench and H_2-membrane setup for internally heated pressure vessels: Description and application for water solubility in basaltic melts. American Mineralogist, 87, 1717–1726.

Blundy, J.D., Melekhova, E., Ulmer, P., Pichavant, M., Humphreys, M.C.S., Ziberna, L., Cerantolo, V., and Brooker, R.A., 2018. Iron redox equilibria in hydrous basaltic melts and Fe^{2+}-Mg exchange between olivine and melt. EMPG-XVI.

Botcharnikov, R.E., Almeev, R.R., Koepke, J., and Holtz, F., 2008. Phase Relations and Liquid Lines of Descent in Hydrous Ferrobasalt: Implications for the Skaergaard

533 Intrusion and Columbia River Flood Basalts. Journal of Petrology, 49, 1687–1727.

534 Bouhifd, M.A., Richet, P., Besson, P., Roskosz, M., and Ingrin, J., 2004. Redox state,
535 microstructure and viscosity of a partially crystallized basalt melt. Earth and Planetary
536 Science Letters, 218, 31–44.

537 Burgess, K.D., Stroud, R.M., Dyar, M.D., and McCanta, M.C., 2016. Submicrometer-scale
538 spatial heterogeneity in silicate glasses using aberration-corrected scanning transmission
539 electron microscopy. American Mineralogist, 101, 2677-2688

540 Buse, B., Kearns, S., 2018. Quantification of Olivine Using Fe Lα in Electron Probe
541 Microanalysis (EPMA). Microscopy and Microanalysis. 24, 1–7.

542 Buse, B., Kearns, S., Clapham, C., and Hawley, D., 2016. Decontamination in the Electron
543 Probe Microanalysis with a Peltier-Cooled Cold Finger. Microscoscopy and
544 Microanalysis, 22, 981–986.

545 Carmichael, I.S.E., 1991. The redox states of basic and silicic magmas: a reflection of their
546 source regions? Contributions to Mineralogy and Petrology, 106, 129–141.

547 Cazaux, J., 1996. Electron Probe Microanalysis of Insulating Materials: Quantification
548 Problems and Some Possible Solutions. X-Ray Spectrometry. 25, 265–280.

549 Cooper, R.F., Fanselow, J.B., and Poker, D.B., 1996. The mechanism of oxidation of a
550 basaltic glass: Chemical diffusion of network-modifying cations. Geochimica et
551 Cosmochimica Acta 60, 3253–3265.

552 Cottrell, E., Kelley, K.A., Lanzirotti, A., and Fischer, R.A., 2009. High-precision
553 determination of iron oxidation state in silicate glasses using XANES. Chemical
554 Geology. 268, 167–179.

555 Cottrell, E., Lanzirotti, A., Mysen, B., Birner, S., Kelley, K.A., Botcharnikov, R.E., Davis,

F.A., and Newville, M., 2018. A mössbauer-based XANES calibration for hydrous basalt glasses reveals radiation-induced oxidation of Fe. American Mineralogist, 103, 489–501.

Creighton, S., Stachel, T., Eichenberg, D., and Luth, R.W., 2010. Oxidation state of the lithospheric mantle beneath Diavik diamond mine, central Slave craton, NWT, Canada. Contributions to Mineralogy and Petrology, 159, 645–657.

Creighton, S., Stachel, T., Matveev, S., Höfer, H., McCammon, C., and Luth, R.W., 2009. Oxidation of the Kaapvaal lithospheric mantle driven by metasomatism. Contributions to Mineralogy and Petrology, 157, 491–504.

de Groot, F., 2001. High-Resolution X-ray Emission and X-ray Absorption Spectroscopy. Chemical Reviews, 101, 1779–1808.

Di Genova, D., Hess, K.U., Oryaelle Chevrel, M., and Dingwell, D.B., 2016. Models for the estimation of Fe^{3+}/Fe_{tot} ratio in terrestrial and extraterrestrial alkali- and iron-rich silicate glasses using Raman spectroscopy. American Mineralogist, 101, 943–952.

Di Genova, D., Kolzenburg, S., Wiesmaier, S., Dallanave, E., Neuville, D.R., Hess, K.U., and Dingwell, D.B., 2017. A compositional tipping point governing the mobilization and eruption style of rhyolitic magma. Nature, 552, 235–238.

Di Genova, D., Romano, C., Giordano, D., and Alletti, M., 2014. Heat capacity, configurational heat capacity and fragility of hydrous magmas. Geochimica et Cosmochimica Acta, 1, 314–333.

Di Genova, D., Romano, C., Hess, K.U., Vona, A., Poe, B.T., Giordano, D., Dingwell, D.B., and Behrens, H., 2013. The rheology of peralkaline rhyolites from Pantelleria Island. Journal of Volcanology and Geothermal Research, 249, 201–216.

Di Genova, D., Sicola, S., Romano, C., Vona, A., Fanara, S., and Spina, L., 2017. Effect of iron and nanolites on Raman spectra of volcanic glasses: A reassessment of existing strategies to estimate the water content. Chemical Geology. 475, 76–86.

Di Muro, A., Métrich, N., Mercier, M., Giordano, D., Massare, D., and Montagnac, G., 2009. Micro-Raman determination of iron redox state in dry natural glasses: Application to peralkaline rhyolites and basalts. Chemical Geology, 259, 78–88.

Dingwell, D.B., and Virgo, D., 1987. The effect of oxidation state on the viscosity of melts in the system Na_2O-FeO-Fe_2O_3-SiO_2. Geochimica et Cosmochimica. Acta 51, 195–205.

Enders, M., McCammon, C.A., Maresch, W. V., and Speer, D., 2000. Ferric/ferrous iron ratios in sodic amphiboles: Mössbauer analysis, stoichiometry-based model calculations and the high-resolution microanalytical flank method. Contributions to Mineralogy and Petrology, 140, 135–147.

Fialin, M., Bézos, A., Wagner, C., and Humler, E., 2004. Quantitative electron microprobe analysis of $Fe^{3+}/\Sigma Fe$: Basic concepts and experimental protocol for glasses. American Mineralogist, 89, 654-662.

Fialin, M., and Wagner, C., 2012. Redox kinetics of iron in alkali silicate glasses exposed to ionizing beams: Examples with the electron microprobe. Journal of Non-Crystalline Solids 358, 1617–1623.

Fialin, M., Wagner, C., Métrich, N., Humler, E., Galoisy, L., and Bézos, A., 2001. $Fe^{3+}/\Sigma Fe$ vs. FeLα peak energy for minerals and glasses: Recent advances with the electron microprobe. American Mineralogist, 86, 456–465.

Fialin, M., Wagner, C., and Pascal, M.-L., 2011. Iron speciation using electron microprobe techniques: application to glassy melt pockets within a spinel lherzolite xenolith.

602 Mineralogy Magazine, 75, 347-362.

603 Fialin, M., Wagner, C., and Pascal, M.-L., 2011. Iron speciation using electron microprobe
604 techniques: application to glassy melt pockets within a spinel lherzolite xenolith.
605 Mineralogy Magazine, 75, 347-362.

606 Fuchs, P., Almeev, R.R., and Klugel, A., 2014. Experimental Constraints on the Formation of
607 Basanites-Phonolite Series (Cumbre Vieja, La Palma). Goldschmidt Conference
608 Abstract.

609 Gopon, P., Fournelle, J., Sobol, P.E., and Llovet, X., 2013. Low-Voltage Electron-Probe
610 Microanalysis of Fe–Si Compounds Using Soft X-Rays. Microscoscopy and
611 Microanalysis, 19, 1698–1708.

612 Hamilton, D.L., Burnham, C.W., and Osborn, E.F., 1964. The Solubility of Water and Effects
613 of Oxygen Fugacity and Water Content on Crystallization in Mafic Magmas. Journal of
614 Petrology, 5, 21–39.

615 Hartley, M.E., Shorttle, O., Maclennan, J., Moussallam, Y., and Edmonds, M., 2017. Olivine-
616 hosted melt inclusions as an archive of redox heterogeneity in magmatic systems. Earth
617 and Planetary Science Letters, 479, 192–205.

618 Hayward, C., 2011. High spatial resolution electron probe microanalysis of tephras and melt
619 inclusions without beam-induced chemical modification. The Holocene 22, 119–125.

620 Herd, C.D.K., 2008. Basalts as Probes of Planetary Interior Redox State. Reviews in
621 Mineralogy and Geochemistry, 68, 527-554.

622 Hofer, H.E., 2002. Quantification of Fe^{2+}/Fe^{3+} by Electron Microprobe Analysis — New
623 Developments. Mössbauer Spectroscopy, 144/145, 239–248.

624 Hofer, H.E., and Brey, G.P., 2007. The iron oxidation state of garnet by electron microprobe:

625 Its determination with the flank method combined with major-element analysis.
626 American Mineralogist, 92, 873–885.

627 Hofer, H.E., Brey, G.P., Schulz-Dobrick, B., and Oberhansli, R., 1994. The determination of
628 the oxidation state of iron by the electron microprobe. European Journal of Mineralogy.
629 6, 407–418.

630 Humphreys, M.C.S., Kearns, S.L., and Blundy, J.D., 2006. SIMS investigation of electron-
631 beam damage to hydrous, rhyolitic glasses: Implications for melt inclusion analysis.
632 American Mineralogist, 91, 667–679.

633 Jarosewich, E., Nelen, J.A., and Norberg, J.A., 1980. Reference Samples for Electron
634 Microprobe Analysis. Geostandards and Geoanalytical Research, 4, 43–47.

635 Klimm, K., Kohn, S.C., O'Dell, L.A., Botcharnikov, R.E., and Smith, M.E., 2012. The
636 dissolution mechanism of sulphur in hydrous silicate melts. I: Assessment of analytical
637 techniques in determining the sulphur speciation in iron-free to iron-poor glasses.
638 Chemical Geology, 322–323, 237–249.

639 Kress, V.C., and Carmichael, I.S.E., 1991. The compressibility of silicate liquids containing
640 Fe_2O_3 and the effect of composition, temperature, oxygen fugacity and pressure on their
641 redox states. Contributions to Mineralogy and Petrology, 108, 82–92.

642 Lafuente, B., Downs, R.T., Yang, H., and Stone, N., 2015. The power of databases: The
643 RRUFF project, in: Armbruster, T., Danisi, R.M. (Eds.), Highlights in Mineralogical
644 Crystallography. De Gruyter, pp. 1–30.

645 Lamb, W.M., Guillemette, R., Popp, R.K., Fritz, S.J., and Chmiel, G.J., 2012. Determination
646 of Fe^{3+}/Fe using the electron microprobe: A calibration for amphiboles. American
647 Mineralogist, 97, 951–961.

Lesne, P., Kohn, S.C., Blundy, J.D., Witham, F., Botcharnikov, R.E., and Behrens, H., 2011. Experimental Simulation of Closed-System Degassing in the System Basalt-H_2O-CO_2-S-Cl. Journal of Petrology, 52, 1737–1762.

Lineweaver, J.L., 1963. Oxygen Outgassing Caused by Electron Bombardment of Glass. Jounral of Applied Physics, 34, 1786.

Malaspina, N., Scambelluri, M., Poli, S., Van Roermund, H.L.M., and Langenhorst, F., 2010. The oxidation state of mantle wedge majoritic garnet websterites metasomatised by C-bearing subduction fluids. Earth and Planetary Science Letters, 298, 417–426.

Matjuschkin, V., Brey, G.P., Höfer, H.E., and Woodland, A.B., 2014. The influence of Fe^{3+} on garnet–orthopyroxene and garnet–olivine geothermometers. Contributions to Mineralogy and Petrology, 167, 972.

McCammon, C.A., 1999. Methods for determination of $Fe^{3+}/\Sigma Fe$ in microscopic samples, in: Gurney, J.L., Gurney, J.., Pascoe, M.D., and Richardson, S.H. (Eds.), Proceedings of the VIIth International Kimberlite Conference, P. H. Nixon Volume. Red Roof Design, Cape Town, South Africa, pp. 540–544.

Metrich, N., and Clocchiatti, R., 1996. Sulfur abundance and its speciation in oxidized alkaline melts. Geochimica et Cosmochimica Acta 60, 4151–4160.

Morgan, G.B., and London, D., 2005. Effect of current density on the electron microprobe analysis of alkali aluminosilicate glasses. American Mineralogist, 90, 1131-1138.

Moussallam, Y., Oppenheimer, C., Scaillet, B., Gaillard, F., Kyle, P., Peters, N., Hartley, M.E., Berlo, K., and Donovan, A., 2014. Tracking the changing oxidation state of Erebus magmas, from mantle to surface, driven by magma ascent and degassing. Earth and Planetary Science Letters, 393, 200–209.

671 Mysen, B.O., Virgo, D., and Seifert, F.A., 1982. The structure of silicate melts: Implications
672 for chemical and physical properties of natural magma. Reviews in Geophysics, 20, 353.

673 Nielsen, C.H., and Sigurdsson, H., 1981. Quantitative methods for electron microprobe
674 analysis of sodium in natural and synthetic glasses. American Mineralogist, 66, 547–
675 552.

676 Nishida, T., 1995. Mössbauer effect in inorganic glasses. Hyperfine Interactions, 95, 23–39.

677 Okumura, S., and Nakashima, S., 2006. Water diffusion in basaltic to dacitic glasses.
678 Chemical Geology, 227, 70–82.

679 Potapkin, V., Chumakov, A.I., Smirnov, G. V., Celse, J.-P., Rüffer, R., McCammon, C., and
680 Dubrovinsky, L., 2012. The ^{57} Fe Synchrotron Mössbauer Source at the ESRF. Journal
681 of Synchrotron Radiation. 19, 559–569.

682 Reed, S.J.., 1975. Electron Microprobe Analysis, Cambridge: Cambridge University Press.

683 Riker, J.M.J., Blundy, J.D., Rust, A.C., Botcharnikov, R.E., and Humphreys, M.C.S., 2015.
684 Experimental phase equilibria of a Mount St. Helens rhyodacite: a framework for
685 interpreting crystallization paths in degassing silicic magmas. Contributions to
686 Mineralogy and Petrology, 170:6.

687 Rowe, M.C., Kent, A.J.R., and Nielsen, R.L., 2007. Determination of sulfur speciation and
688 oxidation state of olivine hosted melt inclusions. Chemical Geology, 236, 303–322.

689 Schuessler, J.A., Botcharnikov, R.E., Behrens, H., Misiti, V., and Freda, C., 2008.
690 Amorphous Materials: Properties, structure, and durability: Oxidation state of iron in
691 hydrous phono-tephritic melts. American Mineralogist, 93, 1493–1504.

692 Smith, D.G.W., and O'Nions, R.K., 1971. Investigations of the $L_{II, III}$ X-ray emission spectra
693 of Fe by the electron microprobe Part I: Some aspects of the Fe $L_{II, III}$ spectra from

metallic iron and haematite. Journal of Physics D: Applied Physics, 4, 147-159.

Stamper, C.C., Melekhova, E., Blundy, J.D., Arculus, R.J., Humphreys, M.C.S., and Brooker, R.A., 2014. Oxidised phase relations of a primitive basalt from Grenada, Lesser Antilles. Contributions to Mineralogy and Petrology. 167, 954.

Ulmer, P., 1989. The dependence of the Fe^{2+}-Mg cation-partitioning between olivine and basaltic liquid on pressure, temperature and composition. Contributions to Mineralogy and Petrology. 101, 261–273.

Vicenzi, E.P., Green, T., and Sie, S., 1994. Effect of oxygen fugacity on trace-element partitioning between immiscible silicate melts at atmospheric pressure: A proton and electron microprobe study. Chemical Geology, 117, 355–360.

Wagner, C., Deloule, E., Fialin, M., and King, P.L., 2008. Dehydrogenation of kaersutitic amphibole under electron beam excitation recorded by changes in $Fe^{3+}/\Sigma Fe$: An EMP and SIMS study. American Mineralogist, 93, 1273–1281.

Wallace, P.J., and Carmichael, I.S.E., 1994. S speciation in submarine basaltic glasses as determined by measurements of S Kα X-ray wavelength shifts. American Mineralogist. 79, 161–167.

Wengorsch, T., Fuchs, P., Almeev, R.R., and Klugel, A., 2012. Revealing true liquid compositions for natural phonolites from Cumbre Vieja volcano, La Palma Island. EMPG-XIV, 143.

Wilke, M., 2005. Fe in magma - An overview. Annals of Geophysics. 48, 609–617.

Wilke, M., Jugo, P.J., Klimm, K., Susini, J., Botcharnikov, R.E., Kohn, S.C., and Janousch, M., 2008. The origin of S^{4+} detected in silicate glasses by XANES. American Mineralogist, 93, 235-240.

Wilke, M., Klimm, K., and Kohn, S.C., 2011. Spectroscopic Studies on Sulfur Speciation in Synthetic and Natural Glasses. Reviews in Mineralogy and Geochemistry, 73, 41–78.

Zhang, C., Almeev, R.R., Hughes, E.C., Borisov, A., Wolff, E., Hofer, H.E., Botcharnikov, R.E., and Koepke, J., in press. Electron microprobe technique for the determination of iron oxidation state in silicate glasses. American Mineralogist.

Appendix

Time-Dependent Ratio Flank Method Protocol

1. Set analytical conditions: 15 kV accelerating voltage, 10 nA beam current and focussed beam. Focus z.
2. Assign spectrometers: TAPs (e.g., TAP, LTAP, TAPH) on F Kα, PETs on K Kα, and LIFs on Fe Kα.
3. Change conditions: 10 μm beam diameter (may need 50 nA beam current for peaking MgF_2).
4. Peak-up spectrometers and set PHA windows: F Kα on MgF_2, K Kα on sanidine, and Fe Kα on basaltic glass.
5. Calculate current Fe $L\alpha_f$ and Fe $L\beta_f$ positions using spectrometer positions from F Kα peak positions.
6. New spectrometer set-up: change TAPs to Fe $L\alpha_f$ and Fe $L\beta_f$.
7. If using Probe for EPMA software: select MAN backgrounds, collect standards (e.g., on sanidine, basaltic glass, NaCl and MgO) otherwise software will not let you export the data.
8. a) If using Probe for EPMA software use Time-Dependent Intensity option: each measurement is 120 s with 24 intervals.

741 b) Otherwise: each measurement 5 s. Either add 24 measurements on the same point
742 or add a line scan of 24 points where the start and end position are the same.
743 9. Collect unknowns and standards (e.g., ten analyses per sample).
744 10. Average data for each sample.
745 11. Process data – R code available in Supplementary Material.
746 12. Produce calibration curve and calculate Fe^{2+}/Fe_T for unknowns.
747
748

List of figure captions

Figure 1 (**a**) Energy level diagram of the electron transitions that generate characteristic Fe X-rays, and (**b**) wavelength spectra of the Fe Lα and Lβ peaks for a reduced, high FeO_T (solid, AR19) and oxidised, low FeO_T (dashed, AR14) silicate glass (Table 1 and Table *2*) plotted using the left-hand axes, and the difference spectrum (dotted, calculated once the wavescans are normalised to their maximum Fe Lα peak intensity) plotted using the right-hand axes. The red box indicates the wavelengths measured for the Peak Shift Method (Fe Lα wavescan). The blue vertical lines indicate optimum wavelength positions measured for the Flank Method, which correspond to the maximum and minimum of the difference spectrum.

Figure 2 (**a**) Total alkalis ($Na_2O + K_2O$) against silica (where SiO_2, Na_2O, and K_2O are normalised to the volatile-free total), and (**b**) Fe^{2+}/Fe_T against FeO_T for samples with known Fe oxidation state. Symbol shape indicates glass composition (Table 1), colour indicates H_2O content, and a black outline indicates known Fe oxidation state; those without an outline have unknown Fe oxidation state. TAS classification abbreviations: PB = picrobasalt, B = basalt, BA = basaltic andesite, A = andesite, D = dacite, TB = trachybasalt, BTA = basaltic trachyandesite, TA = trachyandesite, T = trachyte, R = rhyolite, Ba = basanite, P = phonotephrite, TP = tephriphonolite, and Ph = phonolite.

Figure 3 Wavescans of Fe L for silicate glasses (see Table 2 for compositions). Analytical conditions were: 50 nA beam current and 10 μm beam diameter, whilst the stage moved at 1 $\mu \cdot s^{-1}$. Spectrometer position (L) is shown along the top and equivalent wavelength along the bottom. (**a**) Different FeO_T and Fe oxidation states at 15 kV accelerating voltage, (**b**) different accelerating voltages, (**c**) different accelerating voltages with the intensity normalised to the maximum Fe Lα intensity, and (**d**) difference spectra (AR14 – AR19) at different accelerating voltages, calculated from the normalised spectra, with optimum flank

positions shown (vertical lines). The Fe $L\beta_f/L\alpha_f$ ratio is 0.55 for AR14 and 0.92 for AR19 at 15 kV.

Figure 4 Intensity of K Kα with time. Analytical conditions (accelerating voltage, beam current, beam diameter) shown along the top and sample description on the left-hand side. Symbols and colours as Figure 2a except that open/closed symbol indicates initial Fe oxidation state: open symbols are oxidised ($Fe^{2+}/Fe_T < 0.2$); closed symbols are reduced ($Fe^{2+}/Fe_T > 0.7$).

Figure 5 Intensity of Fe Kα with time. Analytical conditions (accelerating voltage, beam current, beam diameter) shown along the top and sample description on the left-hand side. Symbols and colours as Figure 4.

Figure 6 Intensity ratio of Fe $L\beta_f/L\alpha_f$ with time. Analytical conditions (accelerating voltage, beam current, beam diameter) shown along the top and sample description on the left-hand side. Symbols and colours as Figure 4.

Figure 7 Raman spectra (one spectrum shown for each sample) for (**a**) anhydrous low-silica and (**b**) hydrous glasses, where spectra are grouped, coloured, and offset vertically by average glass composition (labelled under the group of spectra), and intensity is in arbitrary units, and (**c**) selected glasses before and after electron beam irradiation at a 15 kV accelerating voltage, 50 nA beam current, and beam diameter indicated by line style. Black, dashed vertical lines indicate the wavenumber of magnetite, and arrows indicate the wavenumber of haematite.

Figure 8 Rate of change of Fe $L\beta_f/L\alpha_f$ with time at time zero (I'_0) against Total Mobile Cations (TMC, molar sum of $H_2O + Na_2O + K_2O$ per gram of glass), where symbol shape indicates average glass composition (Table 1) and colour indicates H_2O. Analytical

conditions were: 15 kV accelerating voltage, 50 nA beam current, and (**a**) 10 and (**b**) 4 μm beam diameter.

Figure 9 Rate of change of Fe $L\beta_f/L\alpha_f$ with time at time zero (I'_0) against Fe^{2+}/Fe_T for anhydrous low-silica glasses, where symbol colour indicates average glass composition (Table 1) and linear regressions are shown (solid lines). Analytical conditions were: 15 kV accelerating voltage, 50 nA beam current, and 4 μm beam diameter.

Figure 10 Rate of change of Fe $L\beta_f/L\alpha_f$ with time at time zero (I'_0) against Total Mobile Cations (TMC) for hydrous low-silica glasses, where symbol shape and colour indicates average glass composition (Table 1), and open symbols indicate the presence of nanolites. Analytical conditions were: 15 kV accelerating voltage, 50 nA beam current, and 4 μm beam diameter.

Figure 11 Calibration curves derived for two sessions (#2 and 5), where Fe^{2+} is constrained using Fe^{2+}/Fe_T from independent techniques and Fe_T from EPMA. Symbol shape indicates average glass composition (Table 1) and colour indicates H_2O. Analytical conditions were: 15 kV accelerating voltage and 50 nA beam current. (**a**) Low-silica glasses using 10 μm beam diameter, and (**b**) all glasses with separate calibration curves for low-silica (solid) and peralkaline (dashed) glasses (high-silica glasses are shown but not included in the fit), using a 15 μm beam diameter.

Figure 12 EPMA against independently constrained Fe^{2+}/Fe_T collected during all sessions for (**a**) low-silica (43 – 56 wt% SiO_2), (**b**) peralkaline (FSP+PSG), and (**c**) high-silica (69 – 78 wt% SiO_2 – using low-silica glass derived calibration curves) glasses, where symbol shape indicates average glass composition (Table 1) and colour indicates H_2O. Analytical conditions were: 15 kV accelerating voltage, 50 nA beam current, and 4 – 15 μm beam diameter.

819 *Figure 13* Schematic diagram showing the controls on the direction and rate of Fe redox
820 changes in silicate glasses during electron beam irradiation.

This is a preprint, the final version is subject to change, of the American Mineralogist (MSA)
Cite as Authors (Year) Title. American Mineralogist, in press.
DOI: https://doi.org/10.2138/am-2018-6546CCBY

Supplementary Material

Experimental glass synthesis: ETNA glasses

Starting powders were made of a mechanical mixture of albite, anorthite, sanidine, fayalite, wollastonite, SiO_2, MnO, MgO, TiO_2, Fe_2O_3, $Ca_3(PO_4)_2$, and $CaCO_3$, by grinding in an agate mortar. Approximately 50 mg of starting powder was loaded into 3 (diameter) by ~15 (length) mm Au_{80}-Pd_{20} capsules, except ETNA24 where ~500 mg was loaded into a 5 (diameter) by ~30 (length) mm Au_{75}-Pd_{25} capsule, and welded shut. Capsules were immersed in water at 50 ºC then put in an ~100 ºC oven for 10 minutes to check for leaks. Glasses were synthesised (6 capsules at a time, except ETNA24) in an internally-heated pressure vessel (IHPV) for ~18 hours at 1250 ºC and 1, 3, 5 or 7 kbar (see Table 1 for details) using Ar gas as the pressurising medium at the Institut für Mineralogie, Leibniz Universität Hannover, Germany. Experiments were run under intrinsic oxygen fugacity conditions (~NNO+3.5 for H_2O-saturated charges, Berndt et al., 2002). The sample holder is equipped with four S-type thermocouples: two are used to control the furnace temperature and two are used to record the sample temperature. Temperature varied by < 5 ºC during experiments. Pressure variations during the experiment were limited to ±0.02 kbar. Samples were quenched using a rapid-quench device at ~150 °C·s^{-1} (Berndt et al., 2002).

Table 1 Synthesis pressure of experimental samples.

Pressure (kbar)	Sample numbers
1	12, 13, 14, 15, 16, 17
3	1, 2, 3, 6, 7, 11
5	24, 25, 26, 27, 28, 29, 30
7	4, 5, 8, 9, 10

Analytical techniques

Electron Probe Micro-Analysis (EPMA). Major and minor element chemistry of ETNA and AR glasses were measured using the JEOL JXA 8530F Hyperprobe at the School of

Earth Sciences, University of Bristol, UK. Glass chips were mounted in epoxy, ground to a ~1 μm polish then carbon coated (~15 nm thickness). Analytical conditions were: 15 kV accelerating voltage, 10 nA beam current, and 10 μm beam diameter. For quantification, H was included as an element by difference and O was calculated from stoichiometry, with all Fe as FeO. Further analytical details are specified in Table 2 for ETNA glasses and Table 3 for AR glasses.

Table 2 Analytical details for EPMA of ETNA glasses.

	Spectrometer - Crystal				
	1 – TAP	2 – TAP	3 – PETH	4 – LIFH	5 - PETL
1	Si (BCR-2)	Na (BCR-2)	Ca (BCR-2)	Fe (BCR-2)	K (Sanidine)
2	Al (BCR-2)	Mg (BCR-2)	Ti (TiO_2)	Mn (Mn metal)	P (Durango apatite)

Notes: elements were peaked on their standard (given in brackets) and BCR-2 is the USGS basaltic glass standard Columbia River Basalt. Peak counting times were 10 s and high and low background counting times were 5 s each. For each sample, 36 analyses on fresh areas of glass were averaged.

Table 3 Analytical details for EPMA of AR glasses.

	Spectrometer – Crystal				
	1 – PETJ	2 – TAP	3 – TAPH	4 – PETH	5 – LIFL
1	Ca (BCR-2)	Si (BCR-2)	Na (BCR-2)	K (Sanidine)	Fe (BCR-2)
2	Ti (TiO_2)	Al (BCR-2)	Mg (BCR-2)	P (Durango apatite)	Mn (Mn metal)
3	Cl (NaCl)			S (Barite)	

Notes: elements were peaked on their standard (given in brackets), except S which was repeaked on VG2 (Smithsonian microbeam standard) before unknowns were analysed, and BCR-2 is the USGS basaltic glass standard Columbia River Basalt. Peak counting times were 60 s except K which was 120 s. Mean Atomic Number (MAN) backgrounds were used. The first element on each spectrometer had Time-Dependent Intensity (TDI) data collected to extrapolate to time zero in case of element migration. For each sample, three analyses on fresh areas of glass were averaged.

Secondary Ion Mass Spectrometry (SIMS). H_2O was measured in the ETNA glasses using the Cameca IMS-4f at the School of Geosciences, University of Edinburgh, UK. Glass chips were mounted in epoxy, ground to a ~1 μm finish, remounted in indium then gold coated. The analytical target was pre-sputtered over a 20 μm^2 area for three minutes to reduce surface contamination. Prior to H_2O measurements, CO_2 was measured in the same raster pit, but those data are not discussed here. For H_2O analyses, a O^- beam at 15 kV and 5 nA was used to produce positive ions over a 60 μm imaging field which was reduced to ~20 μm using

apertures. During peak centering a rastered 25 μm image field was used. Secondary ions were extracted at 4.5 kV with a 75 kV offset and 40 eV window anda low mass resolution of 400 was used. Species, masses, count times and wait times are detailed in Table 4 and eight cycles were collected for each measurement, although typically only the last six were used. A working curve of H_2O against $^{1}H/^{30}Si$ using background-corrected ^{1}H was constructed using standards containing 0 – 5 wt% H_2O. Samples were analysed 3 – 5 times, except for ETNA24 that was analysed 20 times on three separate chips.

Table 4 Details of SIMS analysis.

Species	0.7	^{1}H	^{23}Na	^{26}Mg	^{30}Si	^{39}K	^{42}Ca	^{47}Ti
Mass	0.7	1.01	22.99	25.98	29.97	28.96	41.96	46.95
Count time (s)	1	4	4	4	2	2	2	2
Wait time (s)	1.5	1	0.2	0.2	0.2	0.2	0.2	0.2

Time-Dependent Ratio Flank Method Calibration Curves. Figure 1 shows the additional calibration curves for sessions #2 – 4 using analytical conditions of 15 kV accelerating voltage, 50 nA beam current, and 4 μm beam diameter. Details of the calibration curves are in Table 5.

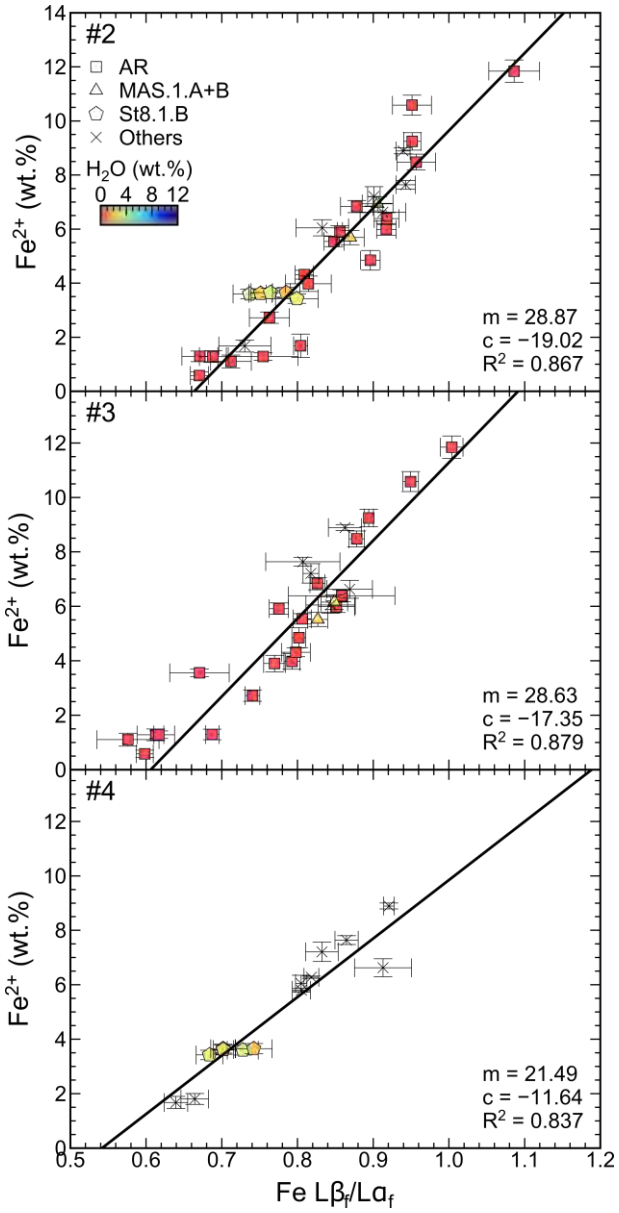

Figure 1 Calibration curves for sessions #2 – 4, with independently constrained Fe^{2+} against corrected Fe $L\beta_f/L\alpha_f$, where symbol shape indicates average glass composition and colour indicates H_2O. Analytical conditions were: 15 kV accelerating voltage, 50 nA beam current, and 4 μm beam diameter. Session number (#) indicated in the top left corner.

Table 5 Results for weighted linear regression for each session.

#	n	*m*	*c*	Adj. R^2	R.S.E. (wt%)
2	32	28.67 ± 2.05	-19.02 ± 1.77	0.87	0.55
3	27	28.63 ± 2.12	-17.35 ± 1.75	0.88	0.50
4	14	21.49 ± 2.72	-11.64 ± 2.16	0.84	0.36

Notes: Data were collected during separate sessions (#) using analytical conditions of a 15 kV accelerating voltage, 50 nA beam current, and 4 μm beam diameter. n is the number of measurements included in the fit. *m* and *c* are the slope and intercept respectively for $Fe^{2+} = m\cdot(\text{Fe } L\beta/L\alpha) + c$. Adj. R^2 is the adjusted R^2. R.S.E. is the residual standard error on estimated Fe^{2+}.

894 **Tables**

895 *Table 1* Normalised (volatile-free), average glass composition for the suites of experimental
896 silicate glasses.

	AR-KLA-1-6-22	AR-SC1	AR-140ox	AR-LS	AR-PF22	AR-BezBA	GRN	ETNA
No.	4	4	3	4	3	4	10	24
SiO_2	44.32	49.42	50.08	51.85	53.53	54.60	46.66	50.75
TiO_2	3.91	2.91	0.99	3.51	1.60	0.99	1.00	1.72
Al_2O_3	13.24	15.37	15.83	12.02	19.66	17.53	13.55	17.63
FeO_T	10.96	11.09	8.68	15.04	5.45	7.92	9.60	10.03
MnO	0.20	0.00	0.17	0.33	0.17	0.18	0.20	0.33
MgO	9.20	6.71	9.81	4.22	2.88	5.92	12.96	6.12
CaO	8.76	11.39	12.11	9.30	4.97	8.56	13.05	7.02
Na_2O	2.99	2.78	2.16	2.93	7.49	2.99	2.16	4.05
K_2O	0.95	0.31	0.07	0.26	3.78	0.95	0.58	1.85
P_2O_5	0.16	0.03	0.08	0.54	0.48	0.16	0.24	0.50
H_2O	0	0	0	0	0	0	[a]0.28 – 3.50	[a]1.58 – 6.07
Fe^{2+}/Fe_T	[c]0.14 – 0.98	[c]0.19 – 0.95	[c]0.18 – 0.97	[c]0.18 – 0.92	[c]0.13 – 0.98	[c]0.20 – 0.91	[e]	n.d.
	MAS.1.A	MAS.1.B	St8.1.B	AMS	FSP	PSG	Y	PSB
No.	6	6	8	3	9	4	7	8
SiO_2	50.86	50.84	51.86	57.72	73.16	69.21	75.37	69.61
TiO_2	1.17	1.18	0.86	0.39	0.43	0.50	0.17	0.35
Al_2O_3	18.91	18.76	19.13	18.40	8.95	9.18	12.25	16.06
FeO_T	11.18	11.19	7.53	4.51	8.14	8.62	3.43	3.30
MnO	n.d.	n.d.	n.d.	0.10	0.35	0.32	0.04	0.06
MgO	3.41	3.17	6.24	1.46	0.17	0.08	0.53	0.78
CaO	9.23	9.41	10.85	4.23	0.44	0.60	1.45	3.05
Na_2O	2.77	2.90	2.67	3.72	4.34	6.52	2.69	4.81
K_2O	1.23	1.29	1.80	7.90	4.08	4.35	4.06	1.87
P_2O_5	n.d.	n.d.	n.d.	0.19	0.00	0.04	0.03	0.10
H_2O	[a]1.58 – 2.86	[a]1.64 – 2.55	[a]1.03 – 3.38	[b]1.29 – 4.78	0	[b]0.72 – 3.55	0	[a]6.35 – 11.50
Fe^{2+}/Fe_T	[c]0.66 – 0.72	[c]0.68 – 0.82	[c]0.63 – 0.68	n.d.	[c]0.17 – 0.76	[c]0.44 – 0.64	[c]0.39 – 0.56	[d]0.48 – 0.77

897 Notes: Oxides (in wt%) are measured using EPMA (all Fe reported as FeO, FeO_T), except
898 H_2O which is measured by [a]SIMS, [b]KFT, or 0 indicates assumed due to experimental
899 conditions. Fe^{2+}/Fe_T is measured by [c]wet chemistry, [d]μXANES or not determined (n.d.). [e]Fe
900 oxidation state measurements may have suffered from oxidation during μXANES and are
901 therefore not used in this study (Cottrell et al., 2018).

Table 2 Fe content and oxidation state of glasses analysed using wavescans.

Sample	AR10	AR14	AR16	AR19	AR20
Glass composition	140ox	PF22	140ox	LS	PF22
FeO_T (wt%)	9.16(24)	5.75(13)	7.85(13)	14.79(19)	4.67(12)
Fe^{2+}/Fe_T	0.18(3)	0.13(3)	0.97(3)	0.92(3)	0.98(3)

Notes: Glass compositions refer to Table 1. FeO_T (all Fe reported as FeO) measured using EPMA and Fe^{2+}/Fe_T using wet chemistry. Errors of one standard deviation corresponding to the last significant figure are shown in brackets.

Table 3 EPMA conditions for Time-Dependent Ratio Fe $L\beta_f/L\alpha_f$ measurements.

Condition	Accelerating voltage (kV)	Beam current (nA)	Beam diameter (μm)	Number of analyses	Total duration (s)
1	15	50	4	10	150
2	15	50	10	10	150
3	15	50	15	10	150
4	15	50	20	10	150
5	15	500	10	1	360
6	30	50	10	10	150

Notes: Conditions 1 – 3 were used to quantify Fe oxidation state, and additional measurements were made at conditions 4 – 6 on AR10, AR16, MAS.1.B4 and PSB63 to investigate redox stability.

Table 4 Glass compositions of AR10, AR16, MAS.1.B4 and PSB63.

	AR10	AR16	MAS.1.B4	PSB63
SiO_2	49.91(30)	50.46(27)	49.72(22)	64.21(32)
TiO_2	0.97(2)	1.00(2)	1.16(3)	0.33(2)
Al_2O_3	15.67(1)	16.08(3)	18.60(5)	14.81(18)
FeO_T	9.16(24)	7.85(13)	10.88(9)	3.26(8)
MnO	0.17(1)	0.18(1)	0.03(1)	0.07(6)
MgO	9.49(2)	10.38(5)	3.28(3)	0.75(6)
CaO	11.89(10)	12.53(5)	8.89(7)	2.91(6)
Na_2O	2.20(2)	1.93(3)	2.89(4)	4.35(28)
K_2O	0.06(1)	0.06(1)	1.25(1)	1.70(12)
P_2O_5	0.08(1)	0.09(1)	0.03(1)	0.10(5)
H_2O	0	0	2.55(13)	7.50(75)
Fe^{2+}/Fe_T	[a]0.18(3)	[a]0.97(3)	[a]0.82(3)	[b]0.76(2)

Notes: Oxides (in wt%) are measured using EPMA (all Fe reported as FeO, FeO_T), except H_2O which is measured by SIMS or 0 indicates assumed due to experimental conditions. Fe^{2+}/Fe_T is measured by [a]wet chemistry or [b]μ-XANES. Errors of one standard deviation corresponding to the last significant figure are shown in brackets.

Table 5 Example of results for weighted linear regression for Fe^{2+} calibration.

#	Beam diameter (μm)	n	*m*	*c*	Adj. R^2	R.S.E. (wt%)
1	10	38	26.87 ± 1.70	-16.08 ± 1.37	0.88	0.51
5	15	10	28.17 ± 1.91	-15.55 ± 1.47	0.96	0.17
5*	15	12	32.94 ± 9.42	-16.96 ± 5.88	0.79	0.05

Notes: Data were collected in sessions #1 and 5 using analytical conditions of a 15 kV accelerating voltage and 50 nA beam current. n is the number of measurements included in the fit. *m* and *c* are the slope and intercept respectively for $Fe^{2+} = m\cdot(Fe\ L\beta/L\alpha) + c$. Adj. R^2

is the adjusted R^2. R.S.E. is the residual standard error on estimated Fe^{2+}. Fits are for low-silica and *peralkaline glasses.

This is a preprint, the final version is subject to change, of the American Mineralogist (MSA)
Cite as Authors (Year) Title. American Mineralogist, in press.
DOI: https://doi.org/10.2138/am-2018-6546CCBY

Figures

Fig.1

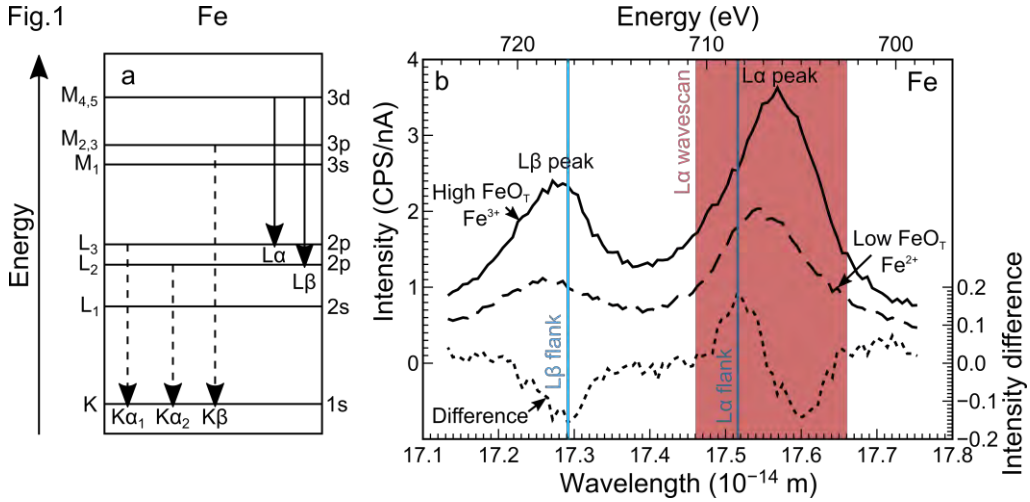

Fig. 2

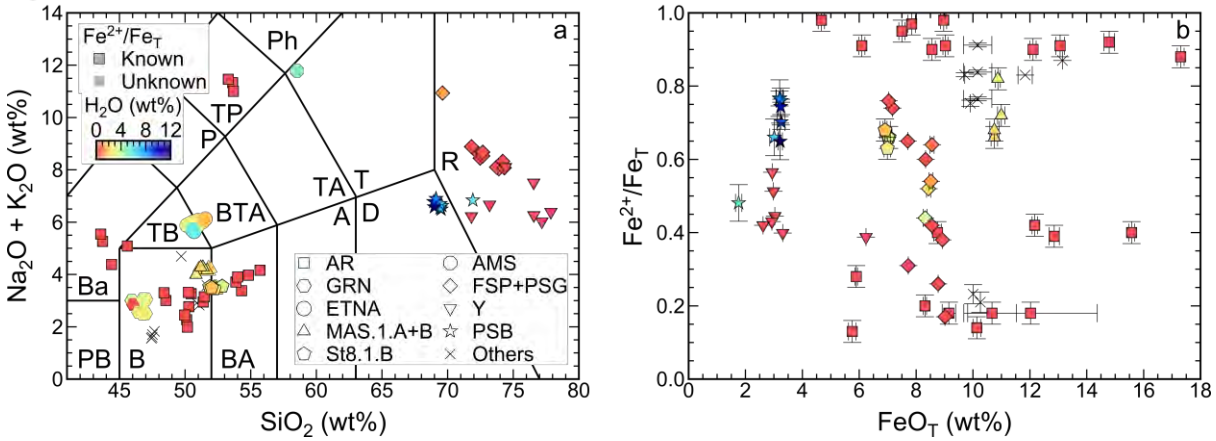

This is a preprint, the final version is subject to change, of the American Mineralogist (MSA)
Cite as Authors (Year) Title. American Mineralogist, in press.
DOI: https://doi.org/10.2138/am-2018-6546CCBY

Fig. 3

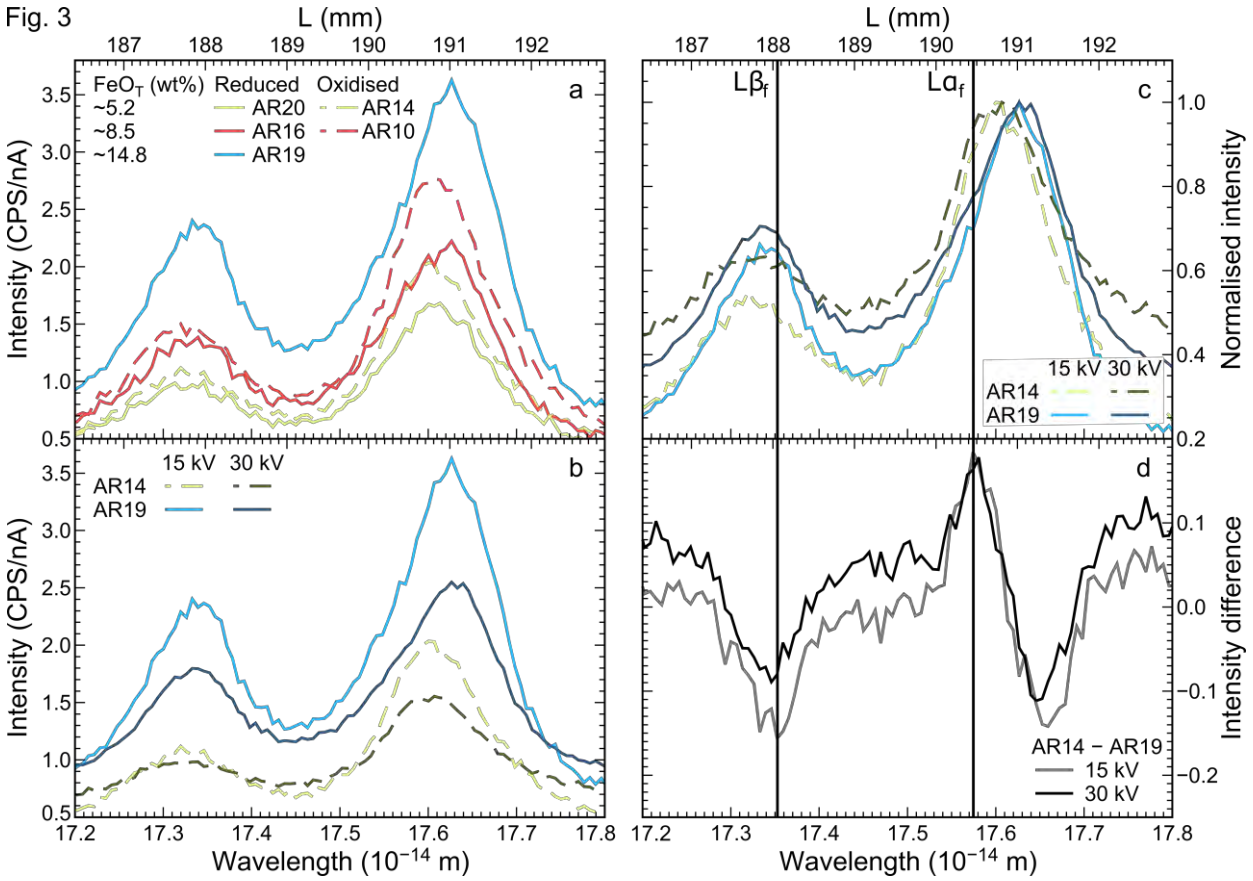

937

Fig. 4

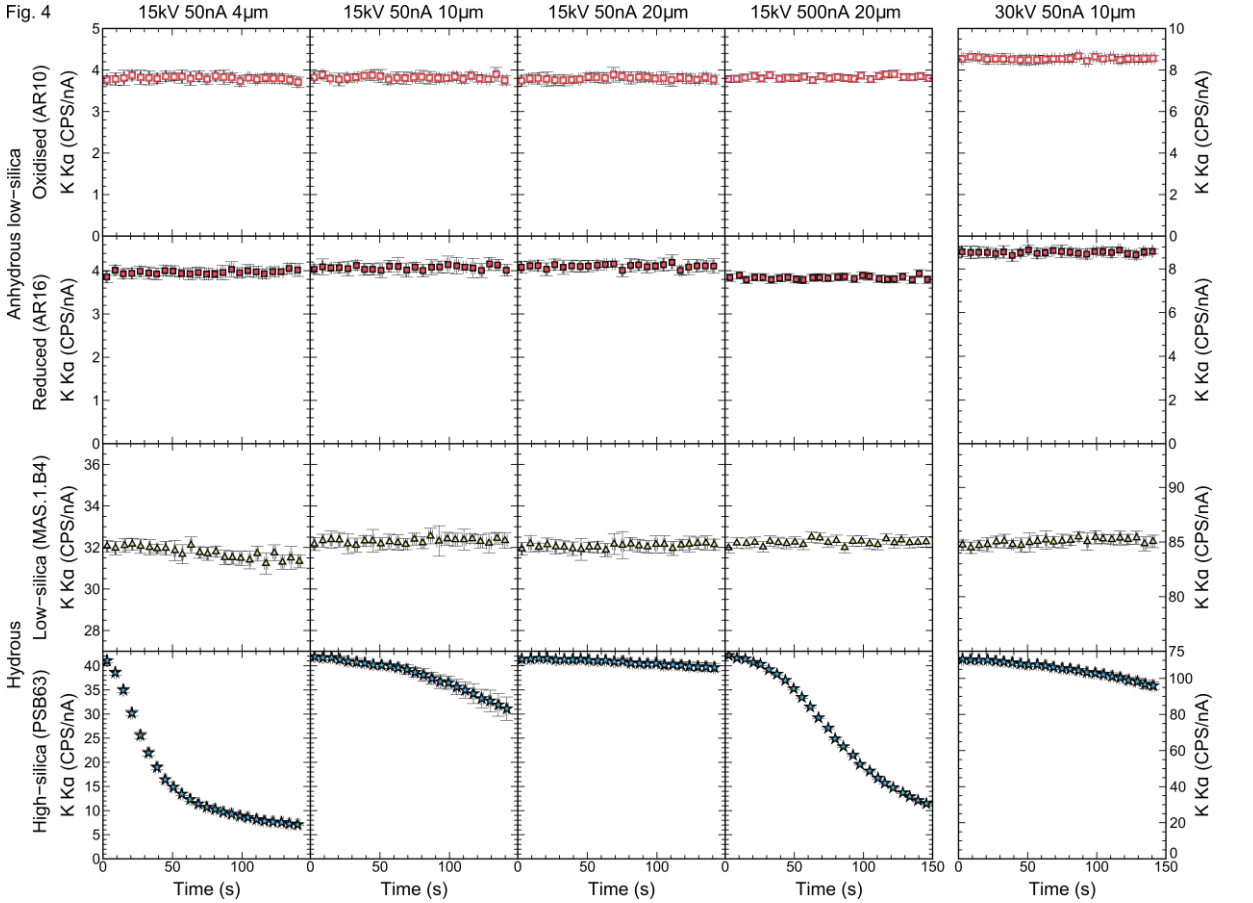

938

This is a preprint, the final version is subject to change, of the American Mineralogist (MSA)
Cite as Authors (Year) Title. American Mineralogist, in press.
DOI: https://doi.org/10.2138/am-2018-6546CCBY

Fig. 5

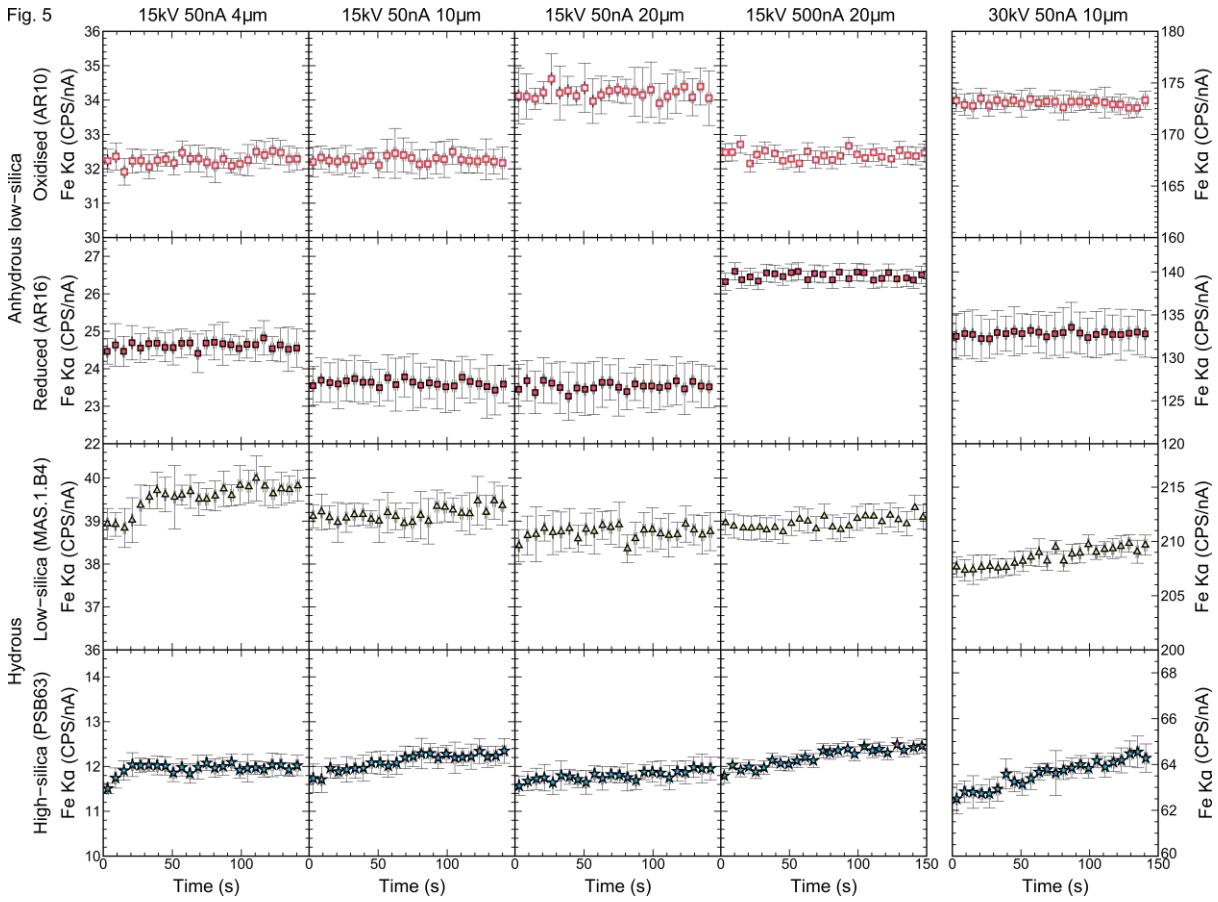

939

Fig. 6

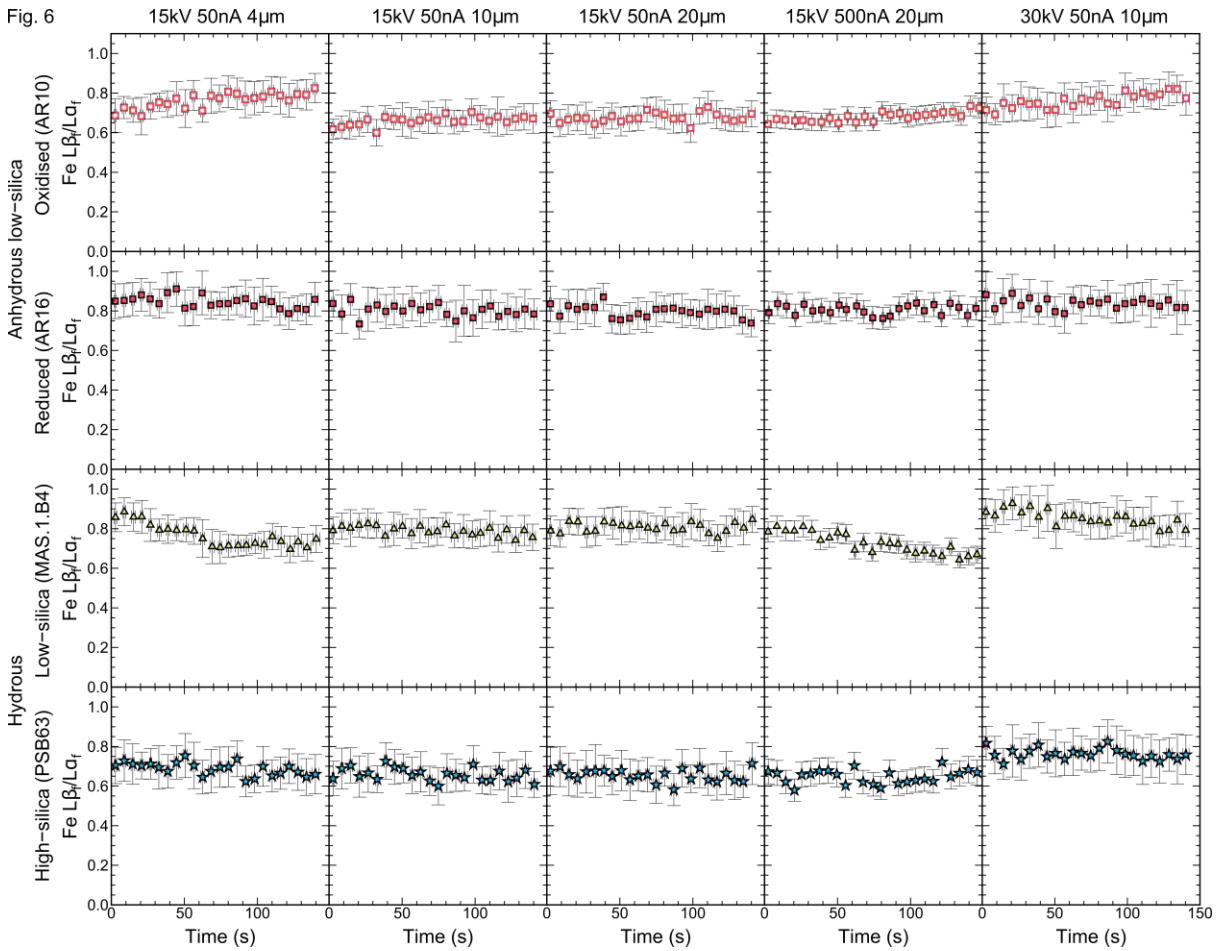

940

This is a preprint, the final version is subject to change, of the American Mineralogist (MSA)
Cite as Authors (Year) Title. American Mineralogist, in press.
DOI: https://doi.org/10.2138/am-2018-6546CCBY

Fig. 7

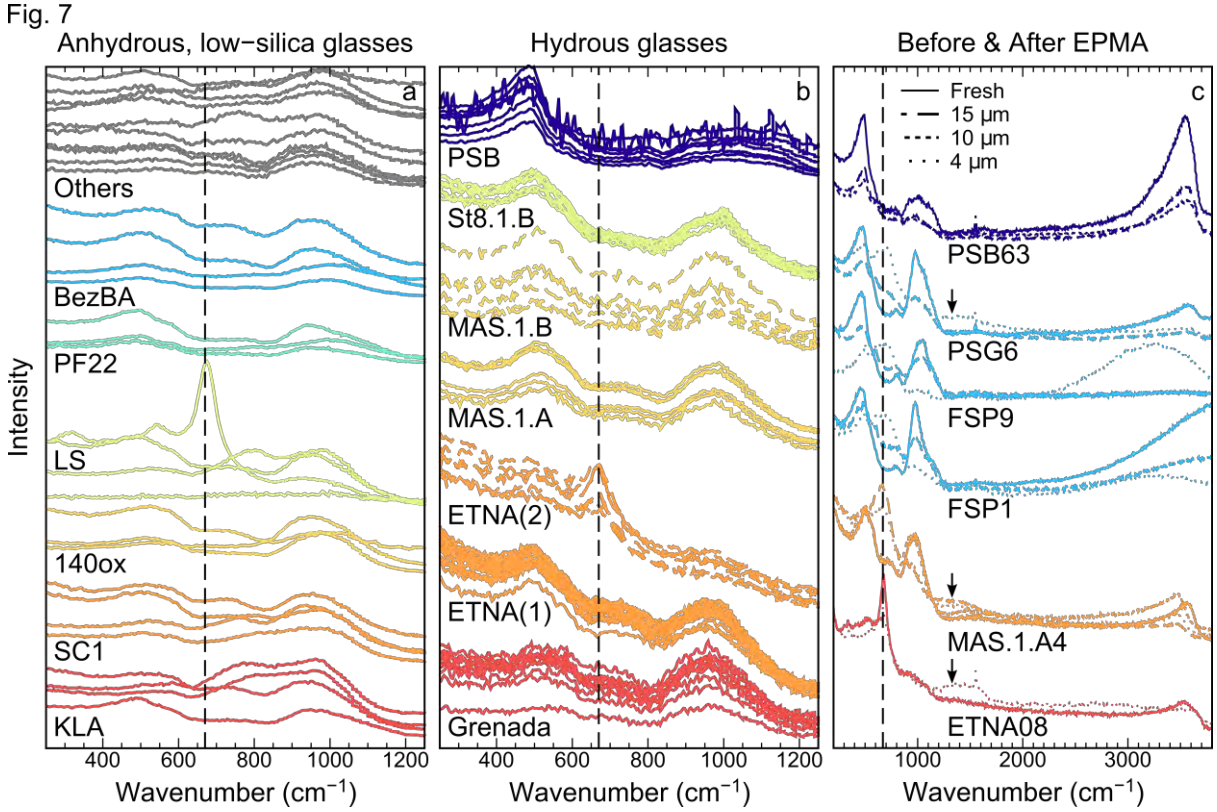

941

942

Fig. 8

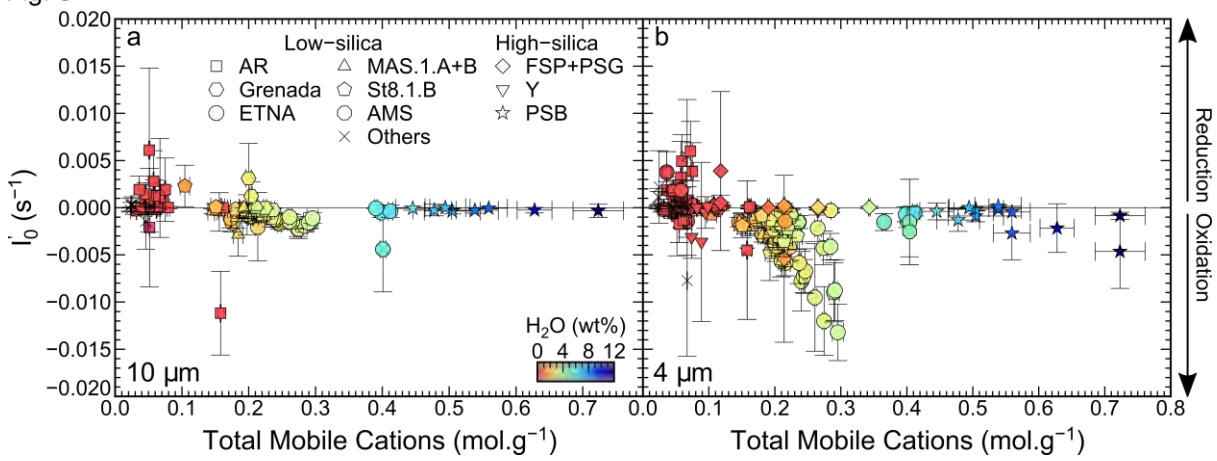

943

Fig. 9

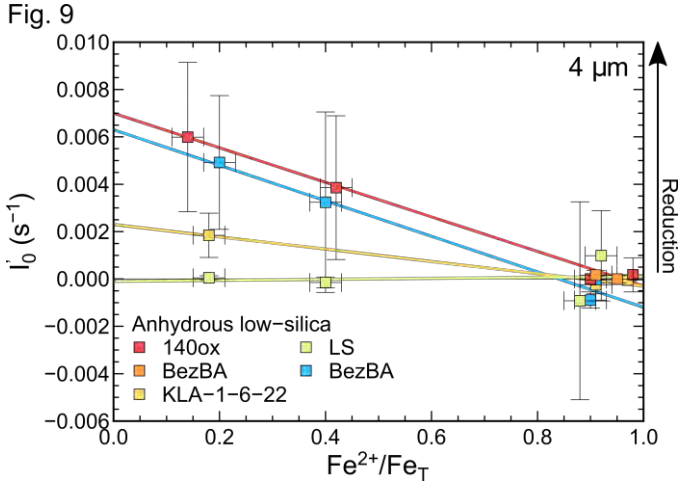

944

This is a preprint, the final version is subject to change, of the American Mineralogist (MSA)
Cite as Authors (Year) Title. American Mineralogist, in press.
DOI: https://doi.org/10.2138/am-2018-6546CCBY

Fig. 10

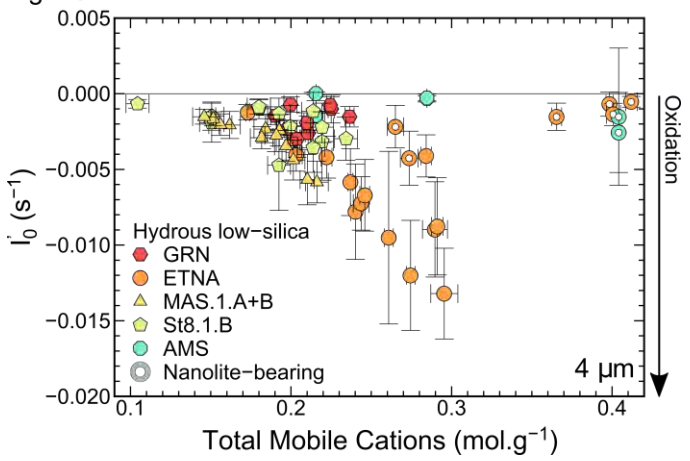

Fig. 11

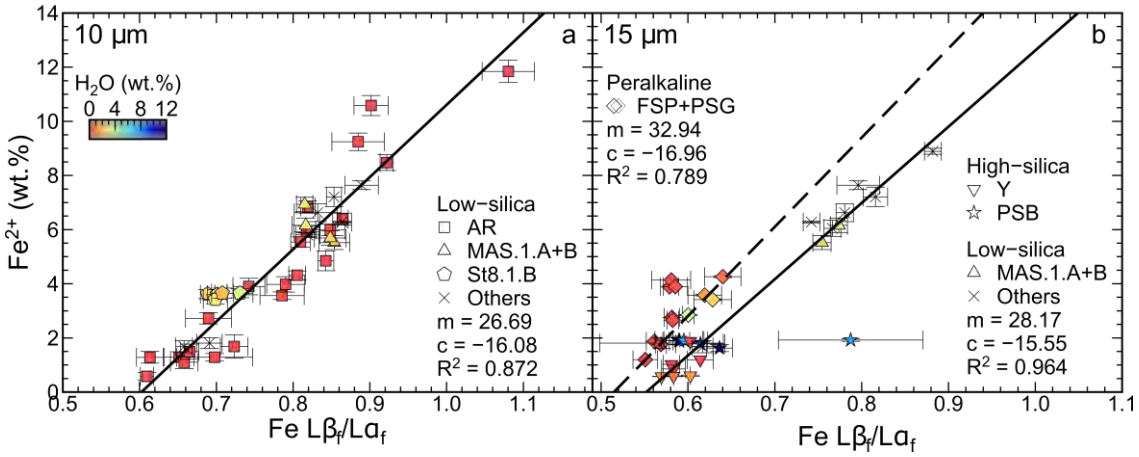

This is a preprint, the final version is subject to change, of the American Mineralogist (MSA)
Cite as Authors (Year) Title. American Mineralogist, in press.
DOI: https://doi.org/10.2138/am-2018-6546CCBY

Fig. 12

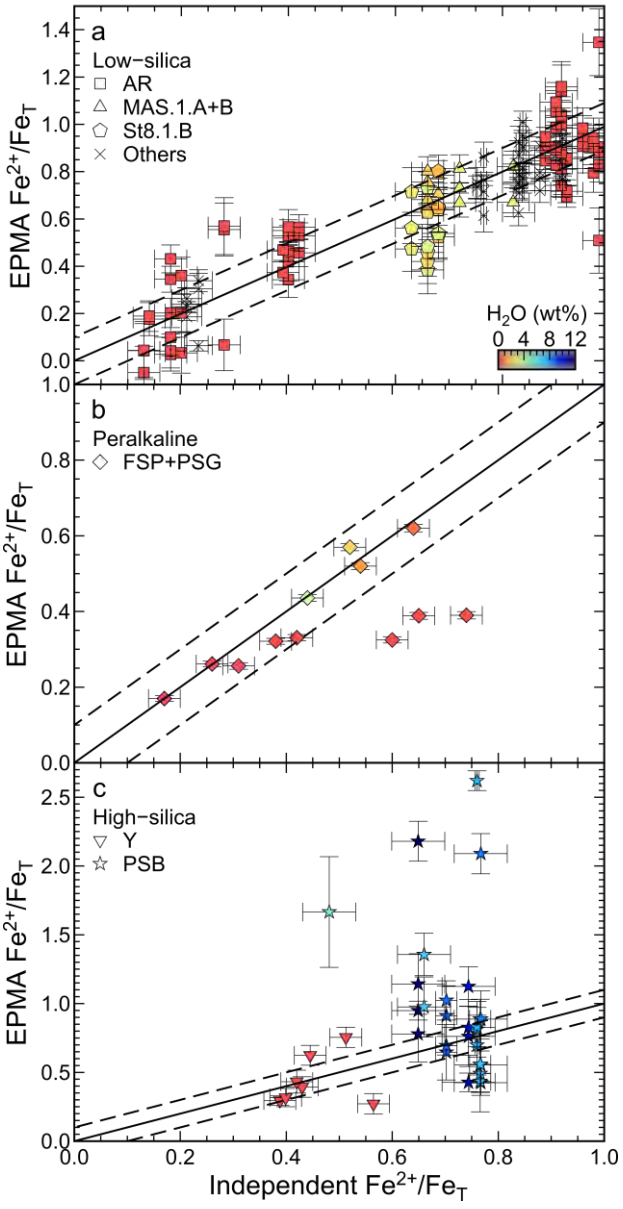

961

Fig. 13

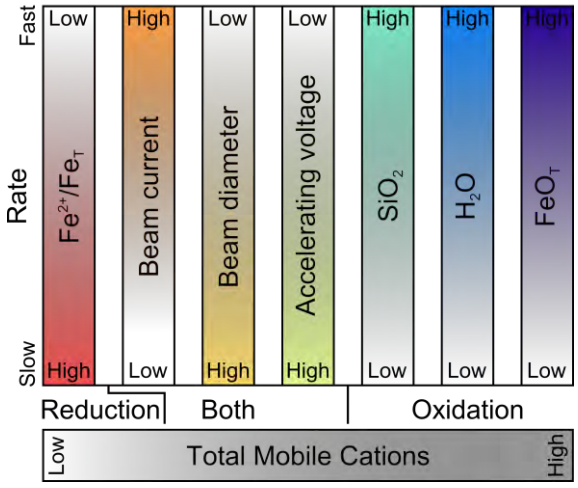

962